A Novel Passivity Model Predictive Control for Predefined-Time Feedforward Compensation in DC Microgrids Feeding Constant Power Loads

Zehua Zhang, *Student Member, IEEE*, Panbao Wang, *Senior Member, IEEE*, Jiyao Zhou, Wei Wang, *Member, IEEE*, and Dianguo Xu, *Fellow, IEEE*

***Abstract*—The negative incremental impedance of constant power loads (CPLs) adversely affects the stable operation of dc microgrids. On the other hand, the power electronic converter should exhibit excellent transient performance when dealing with source-load side disturbances. Hence, this article proposes an adaptive passivity model predictive controller for dc/dc boost converter feeding the CPLs of dc microgrids. First, the predefined-time nonlinear disturbance observer is designed to provide online estimation of unknown and time-varying input voltage and load power. It not only achieves free-setting upper bounds of convergence time, but also reduces sensor needs. Then, combining passivity-based and model predictive control, a composite control that adopts the advantages of both and compensates for the weaknesses of each is proposed. In addition, the proposed composite control loop avoids the complexity of needing to obtain nominal parameters and tuning of multiple-degree-of-freedom parameters, thus providing relatively simple and practical control structure. On this basis, the comprehensive system stability and controller parameter design guidelines are investigated using eigenvalue analysis and discrete-time model bifurcation diagram method. Finally, the simulation and experimental results under multiple scenarios indicate that the proposed control strategy exhibits excellent dynamic performance and robustness with less prior knowledge of the system.**

***Index Terms*—Adaptive passivity model predictive control (APMPC), constant power loads (CPLs), dc/dc boost converter, dc microgrid (MG), predefined-time nonlinear disturbance observer (PTNDO).**

I. Introduction

RECENTLY, microgrids (MGs) have received extensive attention as small-scale power systems that effectively integrate renewable energy sources (RESs), energy storage systems (ESSs), distributed generators (DGs), and modern power electronic loads [1]. Compared to ac MGs, dc MGs have relatively simple control structure that avoids the problem of reactive power flow, synchronization, and frequency [2]. In addition, the dc/dc boost converter reduces redundant energy conversion stages for most power sources and loads with dc nature [3]. Therefore, it is important to explore controllers that achieve fast and stable bus voltage regulation [4].

In dc MGs, the modern loads usually contain resistive loads (RLs) and constant power loads (CPLs). The former are known as passive components that contribute damping to the MGs system. Conversely, the CPLs are tightly regulated power electronic converter loads that consume constant power such that the input side exhibits negative incremental impedance characteristics, thus interacting with the source converter to reduce the system damping Therefore, the highly penetrated CPLs pose a great threat to the stable operation of dc MGs [5], [6].

To eliminate the instability of systems with CPLs, most studies have been performed based on small-signal analysis (SSA) and large-signal analysis (LSA), respectively [7]. The control strategies for SSA are mainly classified into two types: passive damping methods that add passive components to the power circuit [8] and active damping methods that modify the control loop to reshape the system impedance [9]. However, the former increases the weight and cost of the system, and the latter relies on linearized small-signal models, which can only ensure system stability within small ranges of the balance point.

Considering the nonlinear system of the converter and the robustness of the system under large signal disturbances, many advanced control techniques have been proposed to ensure the global stability of the system, such as sliding mode control (SMC) [10], passivity-based control (PBC) [11], backstepping control (BSC) [12], model predictive control (MPC) [13], [14], robust control [15], deep reinforcement learning (DRL) control [16], data-driven control [17], etc. [18], [19]. In [20], an offline explicit MPC method for solving a multiparametric nonlinear programming problem by defining the solution library is proposed, which despite reducing the computational burden, requires sufficiently large memory to ensure robustness under CPL disturbances. In [21], a virtual resistor-based fast robust control strategy is proposed to stabilize the converter of the feeder CPL. Despite the simplicity of the controller design process, the resulting output voltage deviation is not negligible. In [22], the advanced control strategy based on singular perturbation and

Received 3 June 2024; revised 21 September 2024 and 11 November 2024; accepted 22 December 2024. Date of publication 26 December 2024; date of current version 28 January 2025. This work was supported in part by the National Natural Science Foundation of China under Grant 52377173 and in part by the Natural Science Foundation of Heilongjiang Province under Grant LH2022E067. Recommended for publication by Associate Editor M. Molinas. *(Corresponding author: Panbao Wang.)*

Zehua Zhang, Panbao Wang, Wei Wang, and Dianguo Xu are with the School of Electrical Engineering and Automation, Harbin Institute of Technology, Harbin 150001, China (e-mail: 23b906043@stu.hit.edu.cn; wangpanbao@hit.edu.cn; wangwei602@hit.edu.cn; xudiang@hit.edu.cn).

Jiyao Zhou is with the State Grid International Development Company Ltd., State Grid, Beijing 100031, China (e-mail: zhoujiyao@stategrid.com.cn).

Color versions of one or more figures in this article are available at https://doi.org/10.1109/TPEL.2024.3523388.

Digital Object Identifier 10.1109/TPEL.2024.3523388

TABLE I
COMPARISON OF OTHER METHODS AND THE PROPOSED CONTROLLER

Comparison type	[14]	[23]	[26]	[32]	[33]	Proposed control
Disturbance compensation	Power balance	PI	NDO	Finite-time SMDO	Fixed-time SMDO	PTNDO
Parameters to be adjusted	λ_1, λ_2	r_1, k_p, k_i	R_{1d}, R_{2d}, λ_i	k_1, k_2, c, ρ, λ_i, $l_{i,0}$, $l_{i,1}$, $l_{i,2}$, $l_{i,3}$	k_1, k_2, k_3, k_4, k_5, k_6, $\tilde{m}$, $\tilde{n}$, α_1, α_2, β_1, β_2, p, q, m, n	R_V, T_{oi}, ξ_i
Design guidelines	Theoretical analysis and simulation testing	Theoretical analysis and simulation testing	Trial and error and empirical method	Trial and error and empirical method	Trial and error and empirical method	Theoretical analysis and simulation testing
Prior knowledge of system	$i_L(t)$, $v_o(t)$, $i_o(t)$, E_0, L_0, C_0	$i_L(t)$, $v_o(t)$, $E(t)$, P^*, L_0, C_0	$i_L(t)$, $v_o(t)$, L_0, C_0 E_0, P_{CPL0}, R_0	$i_L(t)$, $v_o(t)$ E_0, L_0, C_0	$i_L(t)$, $v_o(t)$ R_0, E_0, L_0, C_0	$i_L(t)$, $v_o(t)$, L_0, C_0
Synthetic complexity	Medium	Medium	Medium	Complex	More complex	Simple
Current limitation	None	None	None	None	None	Yes
Critical power of CPL	None	None	None	None	None	Yes

Synthetic complexity: Determined by combination of parameter tuning numbers, design guidelines and needed prior knowledge of system.

dynamic feedback linearization is proposed. However, the different forms of controllers under different types of loads reduce the generality and practicality. In [23], a proportional-integral based interconnection and damping assignment PBC is proposed to solve the instability problem with CPL. However, when faced with steady-state errors due to disturbances, feedback regulation compensation leads to a slow dynamic response.

To improve the robustness of advanced control strategies, the disturbance observer has received extensive attention as an effective tool for online estimation and feedforward compensation of system uncertainties and disturbances, and can be designed independently of the baseline controller. In [24], an adaptive PBC strategy for estimating CPL power by adaptive extended Kalman filtering (AEKF) is proposed. For BSC [25], PBC [26], MPC [27], and backstepping SMC [28], the composite controller based on nonlinear disturbance observer (NDO) is proposed, where the baseline advanced control strategy ensures the large signal stability of the system, and the NDO is designed to improve the robustness of the controller through online estimation and feed-forward compensation of disturbances. However, the traditional observers only ensure that the estimation error converges asymptotically in infinite time, which is not suitable for sudden load variations in the DG MGs system. In order to improve the speed of disturbance estimation, many disturbance observers with finite time convergence characteristics have been proposed. In [29], an MPC based on higher-order sliding mode observer is proposed to stabilize the feed CPL for dc/dc buck converter. In [30], a composite robust quasi-sliding mode controller based on second-order sliding mode disturbance observer is proposed for a dc microgrid with a stabilized feeder CPL. In [31], an optimal regulation controller combining robust stabilization strategy and DRL is proposed. In [32], an adaptive control strategy based on self-updating gain mechanism is proposed, and the fast regulation capability is achieved through high-order sliding mode observer. However, the upper bound on the finite convergence time for feedforward compensation depends on the initial state of the system, thus limiting the practical applications. In order to avoid the abovementioned problems, Sarrafan et al. [33] proposed a novel fast BSC based on fixed-time disturbance observer to stabilize dc MGs with CPL. However, the complicated relationship between the imprecise time-upper function and the control parameters makes it difficult to realize the desired dynamic response performance [34].

An adaptive passivity model predictive control (APMPC) based on predefined-time nonlinear disturbance observer (PTNDO) is proposed for dc–dc boost converter feeding CPL in dc MGs, which aims to achieve excellent transient and steady-state performances under wide-range operation with a more concise and practical control structure. The proposed controller includes predefined-time feedforward compensation loop and composite control feedback loop. Notably, although the design process of combining the two controllers appears to be complex, the final control law is simple and practical (see discussion in Table I for details). Moreover, the combination of controllers adopts the advantages of both and compensates for their respective weaknesses; the parallel virtual damping of PBC significantly improves the ability of MPC to suppress CPL (see stability analysis for details), while the MPC current loop without weighting coefficients avoids the problems of steady-state deviations, oscillations, and instability that may be caused by the series virtual damping of PBC [24]. To fully reveal the parameter design criteria and stability of proposed controllers, small-signal and large-signal stability analyses are performed. Compared with existing works, the contributions are as follows.

1) An adaptive controller that provides excellent robustness, current limiting, and fast voltage regulation with two types of control combining the advantages of both types to compensate for their respective weaknesses is proposed.
2) According to the best knowledge of authors [24], [25], [26], [27], [28], [29], [30], [31], [32], [33], the first application of PTNDO for dc MGs is proposed. Compared to previous observers converging in infinite, finite, and fixed time, it not only significantly improves the robustness of controller by predefined convergence within time, but also needs only one control parameter independent of the initial state to set an upper bound on the convergence time. Moreover, it improves reliability and reduces system cost compared to sensors obtaining signal.
3) Unlike the traditional PBC voltage loops proposed in [26], which make strict assumptions on disturbances, the

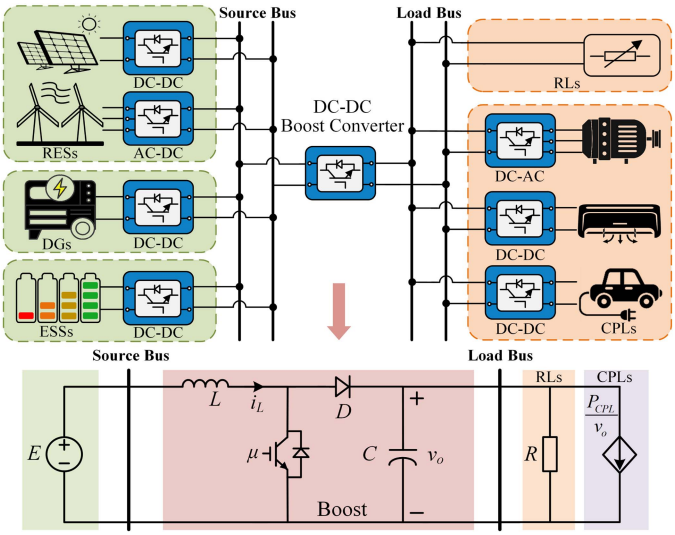

Fig. 1. Typical DC microgrid structure and its equivalent circuit.

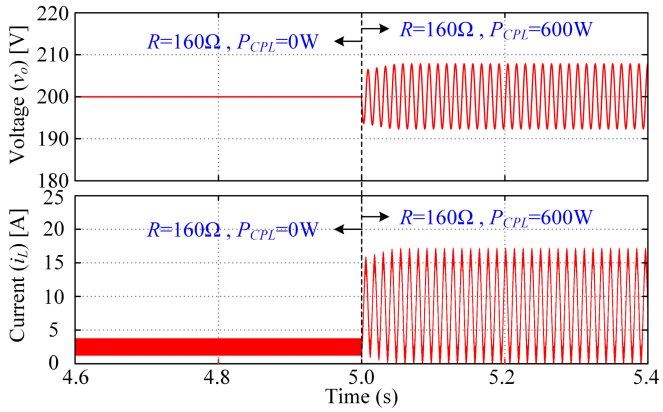

Fig. 2. Dynamic response of DC–DC boost converter under open-loop operation when the CPL power rises from 0 to 600 W, where $E = 100$ V, $L = 1$ mH, $C = 940$ μF, $R = 160$ Ω, $f = 20$ kHz, and $\mu = 0.5$.

proposed PBC voltage loop avoids the use of nominal parameters on the source-load side, improving the applicability of the controller.

4) The MPC current loop without weighting coefficients enables the proposed composite controller feedback loop that only contains single degree-of-freedom parameters, thus providing simple and practical control structure.

The rest of this article is organized as follows. Section II describes the system model and control objectives. The design flow of APMPC based on PTNDO feedforward compensation is presented in Section III. Section IV analyzes the stability of the proposed controller. Simulation and experimental results are given in Sections V and VI, respectively. The conclusion is presented in Section VII.

II. System Model and Problem Formulation

The generic dc microgrid structure and its equivalent circuit are shown in Fig. 1. The source bus is fed through RESs, DGs, and ESSs, while the dc–dc boost converter is used to increase the voltage for load bus energy. The RLs and CPLs act as loads absorbing power from the load bus, while the negative impedance characteristics of the CPLs are detrimental to the system's stability. Therefore, it is necessary to design suitable controllers for the interface converters to achieve stable operation of the dc microgrid.

A. DC Microgrid System Model Description

In this article, the discussed part can be simplified to a system where the dc–dc boost converter feeds the parallel CPLs and RLs. Without loss of generality, the state space model of the dc–dc boost power converter can be expressed as follows:

$$\begin{cases} L\frac{di_L}{dt} = E-(1-\mu)v_o \\ C\frac{dv_o}{dt} = (1-\mu)i_L - \frac{v_o}{R} - \frac{P_{CPL}}{v_o} \end{cases} \Rightarrow \begin{cases} L\frac{di_L}{dt} = \delta_1-(1-\mu)v_o \\ C\frac{dv_o}{dt} = (1-\mu)i_L + \frac{\delta_2}{v_o} \end{cases} \quad (1)$$

where L, C, E, v_o, i_L, μ, R, and P_{CPL} are the inductance value, output-side capacitance value, input voltage, output voltage, inductor current, duty ratio of the switch, RL, and CPL power of the boost converter, respectively. Moreover, $\delta_1 = E$ and $\delta_2 = -P_o$ denote the state variables.

Considering that the converter parameters (L and C) do not deviate during normal operation, conversely, the source-load side parameters are susceptible to external disturbances caused by variations in the operating conditions of the system, which can result the system instability. Moreover, advanced control theory is used to design the system controller and to guarantee robustness by calculating, for instance, the ultimate bound by assuming a given value of uncertainty in the parameters. Therefore, the model with external disturbances and uncertainties is derived by [26]. However, the strict assumption of lumped disturbances leads to the need for the nominal parameters (R_0, P_{CPL0}, and E_0) to be obtained, thus limiting practicality of the model. To avoid the abovementioned problems, this article directly estimates the input voltage E and output power P_o by designing the PTNDO, which not only enhances the practicality of the controller while the predefined time feedforward compensation characteristics significantly improve robustness.

B. Problem Formulation and Control Objectives

Fig. 2 depicts the open-loop dynamic response of the boost converter feeding the CPL and RL. When the CPL steps from 0 to 600 W, i.e., when the negative increasing impedance dominates the system damping, the limit cycle oscillation with unstable equilibrium point is generated. Meanwhile, the highly nonlinear behavior of boost converters and CPLs enables the PI linear control a tradeoff between steady-state margins and dynamic performance [35]. Therefore, it is necessary to design advanced controller with both of these characteristics.

Besides, the strong robustness of the advanced control is another important concern. Although the existing observer technique ensures the controller's difference-free regulation, the convergence speed is important factor that affects the transient performance of the whole system. In particular, dc microgrid

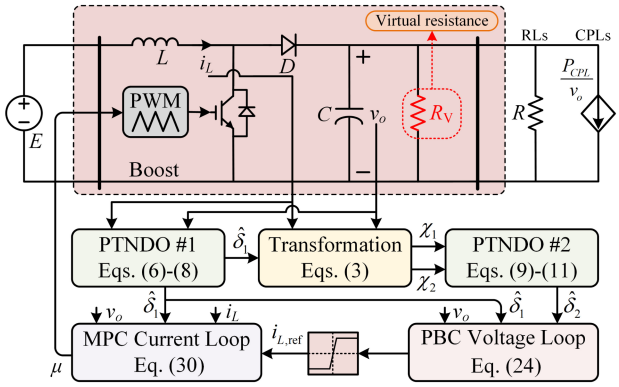

Fig. 3. Boost converter with proposed adaptive passivity MPC block diagram.

systems often face frequent perturbations on the source-load side. Thus, it is necessary to design observers that estimate the source-load side information of the dc microgrid system such that the feedforward compensation signal converges within predefined-time convergence regardless of the initial state, thus significantly improving the robustness of the controller.

III. Proposed Controller Design

In this section, the design procedure and the corresponding stability analysis of the proposed controller are described, which includes PTNDO, PBC voltage loop, and MPC current loop. The detailed control block diagram is shown in Fig. 3.

A. Predefined-Time Nonlinear Disturbance Observer

Considering the practical physical characteristics of dc microgrids, the input voltage and output power terms and their corresponding derivatives are bounded and satisfied.

$$\sup_{t\geq 0}\|\delta_i\|\leq\sigma_1,\ \sup_{t\geq 0}\left\|\dot{\delta}_i\right\|\leq\sigma_2,\ \ i=1,2 \tag{2}$$

where σ_1 and σ_2 are positive constants.

To take the output power in model (1) as a disturbance form and satisfy Brunovsky's standard form, the coordinate transformation is performed by the exact feedback linearization technique, the new model can be expressed as follows:

$$\chi_1=0.5Li_L^2+0.5Cv_o^2,\quad \dot{\chi}_1=Ei_L\underbrace{-P_o}_{\psi_1}=\chi_2+\delta_2 \tag{3}$$

$$\chi_1=0.5Li_L^2+0.5Cv_o^2,\quad \dot{\chi}_1=E_0i_L\underbrace{-P_o+\Delta Ei_L}_{\psi_2} \tag{4}$$

where E_0 is the nominal input voltage. ψ_1 and ψ_2 denote the form of disturbance under different modeling, respectively. According to (3) and (4), when the sensor is used to measure the input voltage E in real time, the disturbance form obtained after coordinate transformation is $\psi_1=-P_o=\delta_2$; when the nominal value of input voltage E_0 is used, the disturbance form obtained after coordinate transformation is $\psi_2=-P_o+\Delta Ei_L\neq\delta_2$, and the accurate estimation of the output power cannot be achieved.

Remark 1: Although the input voltage signal can be real-time measured in control strategy designed based on coordinate transformation, this article designs another PTNDO to estimate and feed-forward compensate input voltage, which can avoid coupling of output power with input voltage disturbance term while without source-side sensor, and can significantly improve robustness of the controller in face of source-side disturbances.

Similarly, the input voltage in model (1) is considered as a disturbance form and transformed to satisfy Brunovsky's standard form, which is expressed as follows:

$$\chi_3=Li_L,\quad \dot{\chi}_3=-(1-\mu)v_o+E=\chi_4+\delta_1 \tag{5}$$

where χ_3 and χ_4 denote state variables.

1) Design of PTNDO: In order to estimate δ_1 in system (1) at predefined time, a reference auxiliary variable is introduced and expressed as follows:

$$\dot{\varphi}_1=\chi_4+\gamma_1z_1,z_1=\chi_3-\varphi_1 \tag{6}$$

where γ_1 is a known positive constant. Then, the PTNDO for estimating the input voltage δ_1 is designed as follows:

$$\hat{\delta}_1=\gamma_1\hat{z}_1+\dot{z}_1 \tag{7}$$

where $\hat{\delta}_1$ is an estimate of the input voltage δ_1. To ensure that the designed PTNDO satisfies Lyapunov stability, the function $\dot{\hat{z}}_1$ is selected as follows:

$$\dot{\hat{z}}_1=\dot{z}_1+\beta_{1,1}\tilde{z}_1+\beta_{2,1}\mathrm{sig}^{1-\xi_1}(\tilde{z}_1)+\beta_{3,1}\mathrm{sig}^{1+\xi_1}(\tilde{z}_1) \tag{8}$$

where $\tilde{z}_1=z_1-\hat{z}_1$ is the estimation error signal, $\beta_{1,1}=\frac{1}{2}\frac{4}{\xi_1T_{o1}}$, $\beta_{2,1}=(\frac{1}{2})^{1-\frac{\xi_1}{2}}\frac{2\alpha_1}{\xi_1T_{o1}\alpha'}$, $\beta_{3,1}=(\frac{1}{2})^{1+\frac{\xi_1}{2}}\frac{2\alpha_2}{\xi_1T_{o1}\alpha'}$, $0<\xi_1<1$, $T_{o1}>0$, $\alpha_1>0$, $\alpha_2>0$ and $\alpha'=\sqrt{\alpha_1\alpha_2}$. T_{o1} denote freely setting predefined-time coefficient, i.e., for any time constant $t>T_{o1}$ satisfying $\hat{z}_1=z_1$ and $\hat{\delta}_1=\delta_1$.

Similarly, in order to estimate δ_2 in system (1), a reference auxiliary variable is introduced and expressed as follows:

$$\dot{\varphi}_2=\chi_2+\gamma_2z_2,z_2=\chi_1-\varphi_2 \tag{9}$$

where γ_2 is a known positive constant. Then, the PTNDO for estimating the output power δ_2 is designed as follows:

$$\hat{\delta}_2=\gamma_2\hat{z}_2+\dot{z}_2 \tag{10}$$

where $\hat{\delta}_2$ is an estimate of the input voltage δ_2. To ensure that the designed PTNDO satisfies Lyapunov stability, the function $\dot{\hat{z}}_2$ is selected as follows:

$$\dot{\hat{z}}_2=\dot{z}_2+\beta_{1,2}\tilde{z}_2+\beta_{2,2}\mathrm{sig}^{1-\xi_2}(\tilde{z}_2)+\beta_{3,2}\mathrm{sig}^{1+\xi_2}(\tilde{z}_2) \tag{11}$$

where $\tilde{z}_2=z_2-\hat{z}_2$ is the estimation error signal, $\beta_{1,2}=\frac{1}{2}\frac{4}{\xi_2T_{o2}}$, $\beta_{2,2}=(\frac{1}{2})^{1-\frac{\xi_2}{2}}\frac{2\alpha_1}{\xi_2T_{o2}\alpha'}$, $\beta_{3,2}=(\frac{1}{2})^{1+\frac{\xi_2}{2}}\frac{2\alpha_2}{\xi_2T_{o2}\alpha'}$, $T_{o2}>0$. T_{o2} denote freely setting predefined-time coefficient, i.e., for any time constant $t>T_{o2}$ satisfying $\hat{z}_2=z_2$ and $\hat{\delta}_2=\delta_2$.

It is worth noting that since the construction of the PTNDO for output power estimation involves input voltage information δ_1. Hence, the selection range of T_{o1} should be $(0, T_{o2})$.

Remark 2: Compared to the existing control strategies that require real-time measurement of input voltage [11] and output current [14], the proposed PTNDO decreases input and output

side sensors through online estimation of the abovementioned variables, thus reducing the system cost and size.

Remark 3: Since the estimated output power and input voltage signals are compensated through the feedforward channel, so the convergence rate of the observer is a major factor affecting the robustness of the whole controller. However, the existing observer techniques [24], [25], [26], [27], [28], [29], [30], [31], [32], [33] are only able to converge in asymptotic time, finite time limited by the initial state, and imprecise fixed time with difficult parameter tuning. Thus, in order to improve the convergence speed and freely setting the upper bound of the convergence time, the PTNDO for dc microgrids is designed. Moreover, the coefficients α_1, α_2, and γ, which indirectly affect the convergence time, are set to 1 to further reduce the difficulty of parameter tuning.

2) Stability Analysis of PTNDO: The stability analysis and convergence characteristics of the designed PTNDO within predefined time are analyzed as follows. First, a continuous positive definite Lyapunov function is constructed as follows:

$$V(\tilde{z}) = 0.5\tilde{z}^2. \tag{12}$$

Combining (6)–(11), the time derivative of (12) about the error trajectory can be expressed as follows:

$$\begin{aligned} V(\tilde{z}) &= \tilde{z}\cdot(-\beta_1\tilde{z} - \beta_2 \mathrm{sig}^{1-\xi}(\tilde{z}) - \beta_3 \mathrm{sig}^{1+\xi}(\tilde{z})) \\ &= -2\left(2\alpha' V(x) + \alpha_1 V^{1-\frac{\xi}{2}}(x) + \alpha_2 V^{1+\frac{\xi}{2}}(x)\right) \Big/ \xi T_o \alpha'. \end{aligned} \tag{13}$$

According to Lemma 1, the mismatch degree of the state variable signal z is eliminated in predefined time and the upper bound on the convergence time can be achieved by free setting of the coefficients T_o. Moreover, the estimation variable $\hat{\delta}$ error can be expressed as follows:

$$\tilde{\delta} = \delta - \hat{\delta} = \delta - \gamma\hat{z} - \dot{z} = \gamma\tilde{z}. \tag{14}$$

According to (14), when the predefined convergence within time of (13) is proved, the estimated variable signal error $\tilde{\delta}$ can also converge to zero within the predefined time.

B. Adaptive PBC Voltage Loop

In this section, the desired objective is to propose an adaptive PBC voltage loop that achieves global equilibrium point stabilization (v_o - $v_{ref} = 0$) with system disturbances and without nominal parameters.

From Fig. 2, it can be seen that increasing RLs improves the system damping, but dissipates additional energy. Therefore, to avoid increasing energy loss and system cost, the passivity control theory (PBC) is applied to inject the parallel virtual impedance R_{v} to reshape the system energy and ensure that the system is strictly passive during the voltage loop design stage.

In order to facilitate the controller design, the state space model is rewritten in the following matrix form:

$$\boldsymbol{H}\dot{\boldsymbol{X}} + [\boldsymbol{G} + \boldsymbol{R}(x)]\boldsymbol{X} = \boldsymbol{\Gamma} \tag{15}$$

where

$$\begin{aligned} \boldsymbol{X} &= \begin{pmatrix} x_1 \\ x_2 \end{pmatrix} = \begin{pmatrix} i_L \\ v_o \end{pmatrix}, \boldsymbol{H} = \begin{pmatrix} L & 0 \\ 0 & C \end{pmatrix}, \boldsymbol{\Gamma} = \begin{pmatrix} E \\ 0 \end{pmatrix} \\ \boldsymbol{G} &= \begin{pmatrix} 0 & (1-\mu) \\ -(1-\mu) & 0 \end{pmatrix}, \boldsymbol{R}(x) = \begin{pmatrix} 0 & 0 \\ 0 & (\frac{1}{R} + \frac{P_{CPL}}{x_2^2}) \end{pmatrix}. \end{aligned} \tag{16}$$

It is obvious that $\boldsymbol{G} = -\boldsymbol{G}^{\mathrm{T}}$ and $\boldsymbol{R} = \boldsymbol{R}^{\mathrm{T}}$, thus (15) satisfies the characteristics of the Euler–Lagrange model which provides a model basis for the design of the PBC. Therefore, the design of the PBC voltage loop follows two stages.

1) Energy Shaping Stage: By adopting $\boldsymbol{X} = \tilde{\boldsymbol{X}} + \boldsymbol{X_d}$ to transform can reshape (15) as follows:

$$\boldsymbol{H}\dot{\tilde{\boldsymbol{X}}} + [\boldsymbol{G} + \boldsymbol{R}(x_m)]\tilde{\boldsymbol{X}} = \boldsymbol{\Gamma} - \left(\boldsymbol{H}\dot{\boldsymbol{X}}_{\boldsymbol{d}} + [\boldsymbol{G} + \boldsymbol{R}(x_d)]\boldsymbol{X_d}\right) \tag{17}$$

where $\boldsymbol{X_d}$ and $\tilde{\boldsymbol{X}}$ denote the reference and disturbance values of $\boldsymbol{X}$, respectively.

2) Damping Injection Stage: This stage modifies the system dissipation function with injecting the virtual damping matrix $\boldsymbol{R_V}\tilde{X}$ at both ends of (17) as follows:

$$\begin{aligned} \boldsymbol{H}\dot{\tilde{\boldsymbol{X}}} + [\boldsymbol{G} + \boldsymbol{R_p}]\tilde{\boldsymbol{X}} = \boldsymbol{\Gamma} - \Big(&\boldsymbol{H}\dot{\boldsymbol{X}}_{\boldsymbol{d}} \\ &+ [\boldsymbol{G} + \boldsymbol{R}(x_d)]\boldsymbol{X_d} - \boldsymbol{R_V}\tilde{\boldsymbol{X}}\Big) \end{aligned} \tag{18}$$

where

$$\begin{aligned} \boldsymbol{R_V} &= \begin{pmatrix} 0 & 0 \\ 0 & \frac{1}{R_{\mathrm{V}}} \end{pmatrix}, \boldsymbol{R}(x_d) = \begin{pmatrix} 0 & 0 \\ 0 & (\frac{1}{R} + \frac{P_{CPL}}{x_{2d}^2}) \end{pmatrix} \\ \boldsymbol{R_p} &= \boldsymbol{R}(x_m) + \boldsymbol{R_V} = \begin{pmatrix} 0 & 0 \\ 0 & (\frac{1}{R_{\mathrm{V}}} + \frac{1}{R} - \frac{P_{CPL}}{x_2 \cdot x_{2d}}) \end{pmatrix}. \end{aligned} \tag{19}$$

To ensure that the system with injected virtual damping matrix satisfies Lyapunov stability, thus exists globally stable equilibrium point ($\tilde{\boldsymbol{X}} = 0$) of the system. The energy function of the system is selected as follows:

$$W = 0.5\tilde{\boldsymbol{X}}^{\boldsymbol{T}}\boldsymbol{H}\tilde{\boldsymbol{X}}. \tag{20}$$

Then, the derivative of the energy function (20) with respect to time can be expressed as follows:

$$\begin{aligned} \dot{W} &= \tilde{\boldsymbol{X}}^{\boldsymbol{T}}\boldsymbol{H}\dot{\tilde{\boldsymbol{X}}} \\ &= \tilde{\boldsymbol{X}}^{\boldsymbol{T}}\left(\boldsymbol{\Gamma} - \left(\boldsymbol{H}\dot{\boldsymbol{X}}_{\boldsymbol{d}} + [\boldsymbol{G} + \boldsymbol{R}(x_d)]\boldsymbol{X_d} - \boldsymbol{R_V}\tilde{\boldsymbol{X}}\right)\right. \\ &\quad \left. -[\boldsymbol{G} + \boldsymbol{R_p}]\tilde{\boldsymbol{X}}\right) \\ &= \tilde{\boldsymbol{X}}^{\boldsymbol{T}}\left(\boldsymbol{\Gamma} - \left(\boldsymbol{H}\dot{\boldsymbol{X}}_{\boldsymbol{d}} + [\boldsymbol{G} + \boldsymbol{R}(x_d)]\boldsymbol{X_d} - \boldsymbol{R_V}\tilde{\boldsymbol{X}}\right)\right) \\ &\quad - \tilde{\boldsymbol{X}}^{\boldsymbol{T}}\boldsymbol{R_p}\tilde{\boldsymbol{X}}. \end{aligned} \tag{21}$$

To make $W(\tilde{\boldsymbol{X}})$ globally stable convergence, it should be ensured that the virtual damping parameter R_{V} is selected to make each element of the matrix $\boldsymbol{R_P}$ positive, and the control

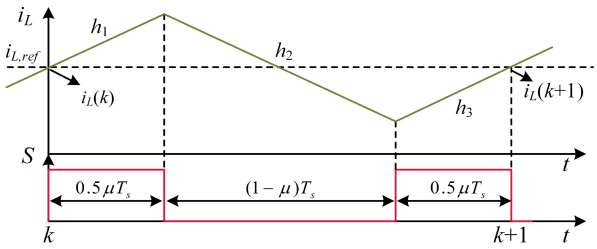

Fig. 4. Inductor current and duty cycle waveforms during switching cycle.

law of the PBC voltage loop is designed as follows:

$$\mathbf{\Gamma} - \left(\boldsymbol{H}\dot{\boldsymbol{X}}_{\boldsymbol{d}} + [\boldsymbol{G} + \boldsymbol{R}(x_d)]\boldsymbol{X}_{\boldsymbol{d}} - \boldsymbol{R}_{\boldsymbol{V}}\tilde{\boldsymbol{X}}\right) = 0. \tag{22}$$

From (22), it is clear that there exists $\dot{x}_{2d} = \dot{v}_{ref} = 0$ during the voltage regulation of PBC, thus the $x_{1d} = i_{L,ref}$ can be written as follows:

$$i_{L,ref} = \frac{v_{ref}^2}{RE} + \frac{P_{CPL}}{E} - \frac{v_{ref}}{R_{\mathrm{V}}E}(v_o - v_{ref}). \tag{23}$$

Although the PBC voltage loop control law obtained by (23) can operate through multiple nominal parameters, the time-varying source-load parameters cause steady-state deviation of control objectives. Therefore, substituting the estimates from (7) and (10) into (23) can be written as follows:

$$i_{L,ref} = -\frac{\hat{\delta}_2}{\hat{\delta}_1} - \frac{v_{ref}(v_o - v_{ref})}{R_{\mathrm{V}}\hat{\delta}_1}. \tag{24}$$

By applying current limiting links after current references can suppress peak currents during start-up and disturbances, thus reducing the current stress of the device.

Remark 4: Compared to the adaptive PBC proposed in [24] and [26], this article proposes an adaptive PBC voltage loop without prerequisites such as input voltage E_0, RL R_0, and CPL power P_{CPL0}. Moreover, with feedforward compensation in predefined time of PTNDO, its robustness is significantly superior to NDO and AEKF, which only provide asymptotic convergence characteristics.

C. Adaptive MPC Current Loop

To avoid the problems of high computational burden and poor robustness of the multistep prediction cycle of MPC, the single-step MPC with adaptive capability is proposed. Notably, the current reference value obtained from the PBC voltage loop is compensated, thus there is no steady-state error problem.

According to model (1), combined with duty cycle $\mu = 1$ or 0 in Fig. 4, the slope of the current can be calculated as follows:

$$\begin{cases} h_1 = h_3 = E(k)/L \\ h_2 = (E(k) - v_o(k))/L \end{cases}. \tag{25}$$

As shown in Fig. 4, based on the inductor current $i_L(k)$ at the current sampling time, the predicted value of inductor current $i_L(k+1)$ at the next time can be expressed as follows:

$$i_L(k+1) = i_L(k) + 0.5\mu h_1 T_s + (1-\mu)h_2 T_s + 0.5\mu h_3 T_s$$
$$= i_L(k) + \frac{E(k)}{L}\mu T_s + \frac{E(k)-v_o(k)}{L}(1-\mu)T_s \tag{26}$$

where T_s is the switching cycle.

The cost function constructed based on the predicted current of a single cycle and reference current can be expressed as follows:

$$J = (i_{L,ref} - i_L(k+1))^2. \tag{27}$$

To obtain optimal variables, (27) partial derivation of μ yields

$$\frac{\partial J}{\partial \mu} = \frac{-2v_o(k)T_s}{L} \cdot \left(i_{L,ref} - i_L(k) - \frac{E(k)}{L}T_s + \frac{(1-\mu)v_o(k)}{L}T_s\right) = 0. \tag{28}$$

Then, the duty cycle μ can be derived as follows:

$$\mu = ((v_o - E)T_s + (i_{L,ref} - i_L)L)/v_o T_s. \tag{29}$$

To achieve an adaptive current loop and to reduce the use of sensors, substituting the estimated value of (7) into (29) yields

$$\mu = ((v_o - \hat{\delta}_1)T_s + (i_{L,ref} - i_L)L)\Big/ v_o T_s. \tag{30}$$

Remark 5: The proposed composite controller composed of PBC voltage loop (24) and MPC current loop (30) only contains one degree-of-freedom (R_{V}), and provides relatively simple and practical control structure with the assistance of the PTNDO.

D. Comparative Discussion

To intuitively compare the proposed controller with existing controllers, the differences between the control methods are shown in Table I. First, the synergy complexity is determined based on the parameters to be adjusted (number and coupling), the completeness of controller design guidelines, and required prior knowledge of the system (number of sensors and nominal parameters). Second, the form of disturbance compensation and the convergence characteristics of disturbance observers are different. In addition, the double-loop structure for voltage and current divides regulation targets, avoids possible stability problems of the single-loop structure, and easily handles the current limitations. Notably, the controller proposed in [14] is only suitable for RLs and is not applicable to CPL.

IV. Stability Analysis

This section is divided into three parts. The first part adopts the eigenvalues of the Jacobian matrix for small-signal stability analysis and explores controller performance through different important parameter variations. In the second part, the system discrete-time model is established and then solved iteratively with consideration of controller time delay to judge the large-signal stability of system through bifurcation diagram obtained. The third part gives the parameter tuning guidelines for the proposed controller.

A. Eigenvalue-Based Small-Signal Stability Analysis

In order to ensure that the proposed controller operates stably according to the desired performance, it is necessary to analyze the stability and provide parameter design guidelines

through eigenvalue traces. However, due to the strong nonlinear characteristics of controller, it is difficult to deduce the closed-loop transfer function by introducing small-signal disturbances. Thus, to avoid complicated solution process, this article adopts the eigenvalues of the Jacobian matrix to evaluate the stability and parameter sensitivity at the operating point of the system, which gives the design guidelines for the controller parameters.

Notably, following the PTNDO response there exists $\hat{\delta}_1 = \delta_1$, $\hat{\delta}_2 = \delta_2$. Moreover, the new error state variables $\omega_1 = v_o\text{-}v_{ref}$, $\omega_2 = i_L\text{-}i_{L,ref}$ are defined. Thus, the closed-loop system model of the proposed controller can be rewritten as follows:

$$\begin{cases} \dot{\omega}_1 = -\frac{1}{C}\left(\frac{1}{R}+\frac{1}{R_V}-\frac{P_{CPL}}{\omega_1 v_{ref}+v_{ref}^2}\right)\omega_1 + \frac{(1-\mu)}{C}\omega_2 \\ \dot{\omega}_2 = \frac{-v_{ref}}{CR_VE}\left(\frac{1}{R}+\frac{1}{R_V}-\frac{P_{CPL}}{\omega_1 v_{ref}+v_{ref}^2}\right)\omega_1 \\ \qquad + \left(\frac{v_{ref}(1-\mu)}{CR_VE}-\frac{1}{T_s}\right)\omega_2 \end{cases}. \quad (31)$$

Before conducting the eigenvalue stability analysis, the system model should be linearized at the equilibrium point, thus (31) the function $f(\omega_1, \omega_2)$ can be defined, and the Taylor polynomial of the $f(\omega_1, \omega_2)$ at (ω_1^*, ω_2^*) can be expressed as follows:

$$f(\omega_1,\omega_2) = f(\omega_1^*,\omega_2^*) + R_n(\omega) + (\omega_1-\omega_1^*)f'_{\omega_1}(\omega_1^*,\omega_2^*) + (\omega_2-\omega_2^*)f'_{\omega_2}(\omega_1^*,\omega_2^*) \quad (32)$$

where $R_n(\omega)$ is higher-order infinitesimal expanding term of $(\omega-\omega^*)$. By ignoring the higher-order terms $R_n(\omega)$ of the studied system, the function near the steady state can be expressed as follows:

$$f(\omega_1,\omega_2) \approx f(\omega_1^*,\omega_2^*) - \omega_1^* f'_{\omega_1}(\omega_1^*,\omega_2^*) - \omega_2^* f'_{\omega_2}(\omega_1^*,\omega_2^*) + \omega_1 f'_{\omega_1}(\omega_1^*,\omega_2^*) + \omega_2 f'_{\omega_2}(\omega_1^*,\omega_2^*). \quad (33)$$

Substituting (31) into (33), the Jacobian matrix J_m can be denoted as follows:

$$J_m = \begin{bmatrix} J_{m11} & J_{m12} \\ J_{m21} & J_{m22} \end{bmatrix} = \begin{bmatrix} \frac{\partial f_1(\omega_1,\omega_2)}{\partial \omega_1} & \frac{\partial f_1(\omega_1,\omega_2)}{\partial \omega_2} \\ \frac{\partial f_2(\omega_1,\omega_2)}{\partial \omega_1} & \frac{\partial f_2(\omega_1,\omega_2)}{\partial \omega_2} \end{bmatrix} \quad (34)$$

where J_{m11}-J_{m22} are deduced as follows:

$$\begin{cases} J_{m11} = -\frac{1}{C}\left(\frac{1}{R}+\frac{1}{R_V}-\frac{P_{CPL}}{v_{ref}^2+v_{ref}\omega_1^*}\right) - \frac{P_{CPL}v_{ref}\omega_1^*}{C(v_{ref}^2+v_{ref}\omega_1^*)^2} \\ \qquad -\frac{\partial\mu}{\partial\omega_1}\cdot\frac{\omega_2^*}{C} + \frac{ET_s+\omega_2^*L}{CT_s(\omega_1^*+v_{ref})}\cdot\frac{v_{ref}}{R_VE} \\ J_{m12} = \frac{ET_s+\omega_2^*L}{CT_s(\omega_1^*+v_{ref})} - \frac{\partial\mu}{\partial\omega_2}\cdot\frac{\omega_2^*}{C} \\ J_{m21} = -\frac{v_{ref}}{CR_VE}\left(\frac{1}{R}+\frac{1}{R_V}-\frac{P_{CPL}}{v_{ref}^2+v_{ref}\omega_1^*}\right) \\ \qquad -\frac{P_{CPL}v_{ref}^2\omega_1^*}{CR_VE(v_{ref}^2+v_{ref}\omega_1^*)^2} \\ \qquad -\frac{\partial\mu}{\partial\omega_1}\cdot\frac{v_{ref}\omega_2^*}{CR_VE} + \left(\frac{(ET_s+\omega_2^*L)v_{ref}}{CR_VET_s(\omega_1^*+v_{ref})}-\frac{1}{T_s}\right)\cdot\frac{v_{ref}}{R_VE} \\ J_{m22} = \left(\frac{(ET_s+\omega_2^*L)v_{ref}}{CR_VET_s(\omega_1^*+v_{ref})}-\frac{1}{T_s}\right) - \frac{\partial\mu}{\partial\omega_2}\cdot\frac{v_{ref}\omega_2^*}{CR_VE} \end{cases} \quad (35)$$

where the derivatives of the state variables ω_1 and ω_2 with respect to the optimal control variable duty cycle μ can be derived from (30) as follows:

$$\begin{cases} \frac{\partial\mu}{\partial\omega_1} = \frac{(ET_s+\omega_2^*L)T_s-(v_{ref}LT_s(\omega_1^*+v_{ref})/R_VE)}{[(\omega_1^*+v_{ref})T_s]^2} \\ \frac{\partial\mu}{\partial\omega_2} = -\frac{L}{(\omega_1^*+v_{ref})T_s} \end{cases}. \quad (36)$$

In order to ensure the accuracy of the studied model, the expansion points ω_1^* and ω_2^* should be zero. The parameters of the Jacobian matrix can be obtained as follows:

$$J_m = \begin{bmatrix} J_{m11} & J_{m12} \\ J_{m21} & J_{m22} \end{bmatrix} = \begin{bmatrix} \frac{P_{CPL}}{v_{ref}^2}-\frac{1}{CR} & \frac{E}{Cv_{ref}} \\ \frac{P_{CPL}}{CR_VEv_{ref}}-\frac{v_{ref}}{CR_VER}-\frac{v_{ref}}{R_VT_sE} & \frac{1}{CR_V}-\frac{1}{T_s} \end{bmatrix}. \quad (37)$$

By analyzing the position of the eigenvalues of the Jacobian matrix in the s-plane, the small-signal stability and performance indicators of the system can be evaluated.

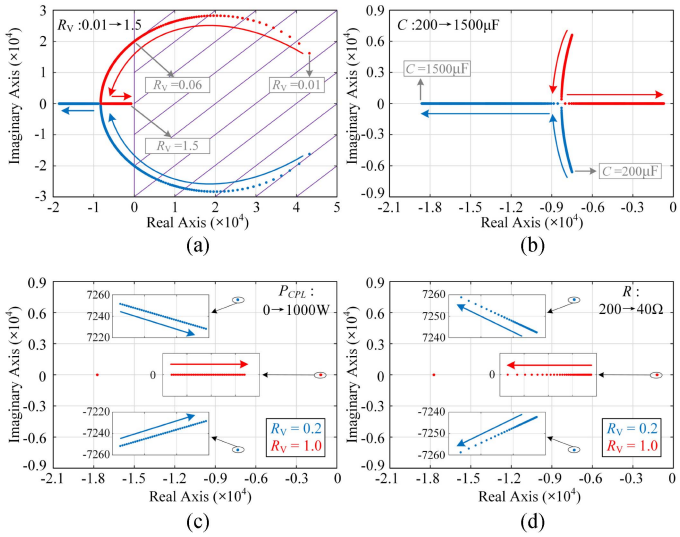

Fig. 5. Eigenvalues traces of closed-loop systems under important parameter variations. (a) R_V variation from 0.01 to 1.5. (b) C variation from 200 to 1500 μF. (c) P_{CPL} variation from 0 to 1000 W at R_V 0.2 and 1.0, respectively. (d) R variation from 200 to 40 Ω at R_V 0.2 and 1.0, respectively.

Fig. 5(a)–(d) depict the eigenvalue trajectories of the system as the parameters R_V, C, P_{CPL}, and R are variation, respectively. To ensure the accuracy of the model, the control variable method is used in this article, i.e., the parameters are consistent with Table II except for the parameters under study.

From Fig. 5(a), when the virtual damping R_V increases from 0.01 to 0.06, the dominant eigenvalue is always located in the right half-axis of plane with system unstable. As R_V increases, the eigenvalue moves across and away from imaginary axis closer to the real axis, which indicates that the system is stable and the damping ratio increases, and the amount of overshoot and oscillation decreases. However, when R_V exceeds certain range, the dominant eigenvalue moves closer to imaginary axis, which leads to decrease in the convergence speed of the system.

From Fig. 5(b), the dominant eigenvalue is gradually close to the real axis as the capacitance C increases, which indicates the decrease of the system oscillation and overshoot. However, when

TABLE II
SYSTEM PARAMETERS CONFIGURATION

Description	Variables	Values
Converter input voltage	E	100 V
Desired output bus voltage	v_{ref}	200 V
Converter inductance value	L	1 mH
Converter capacitance value	C	940 μF
Switching frequency	f_{sw}	20 kHz
PBC virtual damping gain	R_V	1
MPC projective period	T_s	$1/f_{sw}$
Gains for PTNDO #1 ($i = 1, 2$)	T_{oi}	0.01, 0.02
Gains for PTNDO #2 ($i = 1, 2$)	ξ_i	0.8

the capacitance C continues to increase, the dominant eigenvalues gradually approach the imaginary axis, which gradually reduces the convergence speed of the system.

From Fig. 5(c) and (d), as the load power increases, the dominant eigenvalue for CPL variation gradually moves closer to the imaginary axis, while the dominant eigenvalue for RL variation gradually moves away from the imaginary axis, but all poles are located in left half-plane, which indicates that the proposed controller ensures the system stability.

Based on the abovementioned analysis, the following is summarized.

Conclusions1: The selection of the virtual damping for the single-degree-of-freedom parameter of the proposed controller is critical for the system stability and transient performance, an appropriate R_V is helpful for fast convergence and no overshoots of the system.

Conclusions2: The wide range of capacitance values ensures the stability of the proposed controller, but the selection of parameters affects the transient performance of the system.

Conclusions3: Although CPL is detrimental to the stability of the system, the system can maintain stable operation after using the proposed controller and designing the parameters according to conclusions 1.

B. Bifurcation-Based Large Signal Stability Analysis

Although the stability of the proposed controller is verified in Section IV-A, it is only applicable to system parameter analysis and stability estimation under small-signal disturbances, and is not fully satisfied in dc MGs with large-signal disturbances. In addition, the estimation of the maximum power point of the CPL is difficult with the large-signal stability analysis method based on the Lyapunov function. Therefore, in order to perform large-signal stability analysis without linearization of the system, we construct discrete-time system model including switching effects to characterize the nonlinearity of MGs while reducing the model deviation at high cut-off frequencies [36], [37].

In this section, in order to obtain the next moment state variables without linearization, we discretize the PWM period through sufficiently small step size to derive discrete-time system model considering switching effect, as shown in Fig. 6. Where T_s and T_e are the PWM period and discretization period,

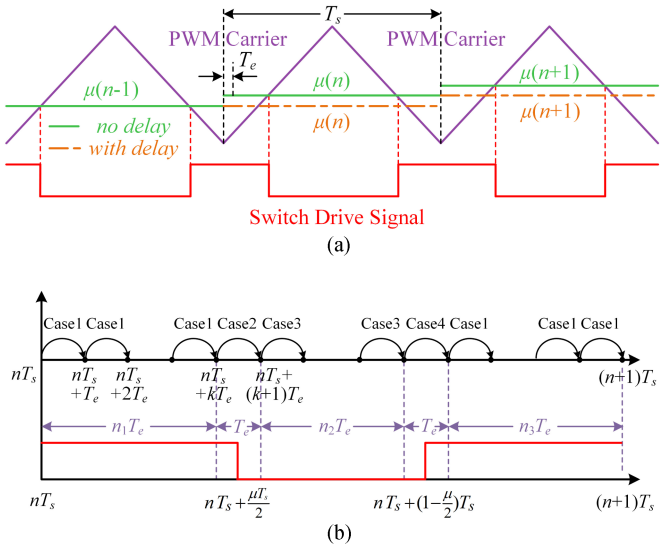

Fig. 6. Iterative calculation of discrete-time model considering switching effect. (a) Discretization process for PWM with period T_e. (b) Calculation process during discrete PWM period.

respectively. Compared to [38], which adopts the Euler method with first-order accuracy, this article adopts the Runge–Kutta method with fourth-order accuracy to satisfy the requirement of high accuracy in the practical. The method achieves higher accuracy in numerical solution by taking the slopes of several points in interval and then weighting them as the average slope.

First, the state variables of discrete-time converter model are defined as follows:

$$\boldsymbol{X}_t(k) = \begin{bmatrix} i_{L\_t}(k) & v_{o\_t}(k) \end{bmatrix}^{\mathrm{T}}. \tag{38}$$

When the drive signal is above the triangular carrier and does not intersect, the next momentary state variable can be deduced from the fourth-order Runge–Kutta as follows:

$$\begin{cases} i_{L\_t}(k+1) = i_{L\_t}(k) + \frac{T_e}{6}(H_{11} + 2H_{12} + 2H_{13} + H_{14}) \\ v_{o\_t}(k+1) = v_{o\_t}(k) + \frac{T_e}{6}(H_{21} + 2H_{22} + 2H_{23} + H_{24}) \end{cases} \tag{39}$$

where

$$\begin{aligned} \begin{bmatrix} H_{11} \\ H_{21} \end{bmatrix} &= \dot{\boldsymbol{X}}\left(\begin{bmatrix} i_{L\_t}(k) \\ v_{o\_t}(k) \end{bmatrix}, \mu = 1 \right) \\ \begin{bmatrix} H_{12} \\ H_{22} \end{bmatrix} &= \dot{\boldsymbol{X}}\left(\begin{bmatrix} i_{L\_t}(k) \\ v_{o\_t}(k) \end{bmatrix} + \frac{T_e}{2} \begin{bmatrix} H_{11} \\ H_{21} \end{bmatrix}, \mu = 1 \right) \\ \begin{bmatrix} H_{13} \\ H_{23} \end{bmatrix} &= \dot{\boldsymbol{X}}\left(\begin{bmatrix} i_{L\_t}(k) \\ v_{o\_t}(k) \end{bmatrix} + \frac{T_e}{2} \begin{bmatrix} H_{12} \\ H_{22} \end{bmatrix}, \mu = 1 \right) \\ \begin{bmatrix} H_{14} \\ H_{24} \end{bmatrix} &= \dot{\boldsymbol{X}}\left(\begin{bmatrix} i_{L\_t}(k) \\ v_{o\_t}(k) \end{bmatrix} + T_e \begin{bmatrix} H_{13} \\ H_{23} \end{bmatrix}, \mu = 1 \right). \end{aligned} \tag{40}$$

When the drive signal is below the triangular carrier and does not intersect, the next momentary state variable can be deduced

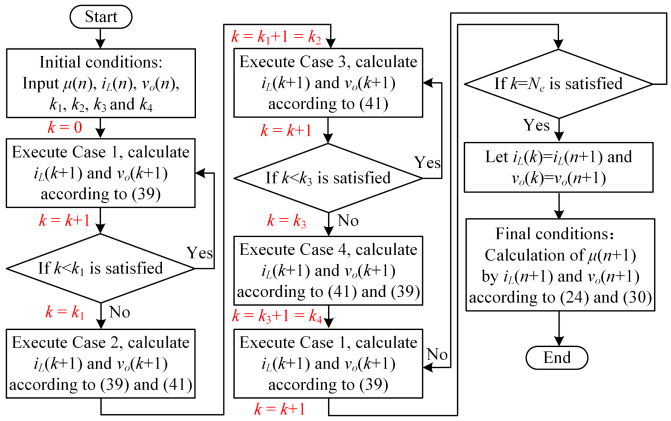

Fig. 7. Calculation flowchart of the proposed controller and discrete-time system model during a switching period.

from the fourth-order Runge–Kutta as follows:

$$\begin{cases} i_{L\_t}(k+1) = i_{L\_t}(k) + \frac{T_e}{6}(L_{11} + 2L_{12} + 2L_{13} + L_{14}) \\ v_{o\_t}(k+1) = v_{o\_t}(k) + \frac{T_e}{6}(L_{21} + 2L_{22} + 2L_{23} + L_{24}) \end{cases} \tag{41}$$

where

$$\begin{aligned} \begin{bmatrix} L_{11} \\ L_{21} \end{bmatrix} &= \dot{\boldsymbol{X}}\left(\begin{bmatrix} i_{L\_t}(k) \\ v_{o\_t}(k) \end{bmatrix}, \mu = 0 \right) \\ \begin{bmatrix} L_{12} \\ L_{22} \end{bmatrix} &= \dot{\boldsymbol{X}}\left(\begin{bmatrix} i_{L\_t}(k) \\ v_{o\_t}(k) \end{bmatrix} + \frac{T_e}{2} \begin{bmatrix} L_{11} \\ L_{21} \end{bmatrix}, \mu = 0 \right) \\ \begin{bmatrix} L_{13} \\ L_{23} \end{bmatrix} &= \dot{\boldsymbol{X}}\left(\begin{bmatrix} i_{L\_t}(k) \\ v_{o\_t}(k) \end{bmatrix} + \frac{T_e}{2} \begin{bmatrix} L_{12} \\ L_{22} \end{bmatrix}, \mu = 0 \right) \\ \begin{bmatrix} L_{14} \\ L_{24} \end{bmatrix} &= \dot{\boldsymbol{X}}\left(\begin{bmatrix} i_{L\_t}(k) \\ v_{o\_t}(k) \end{bmatrix} + T_e \begin{bmatrix} L_{13} \\ L_{23} \end{bmatrix}, \mu = 0 \right). \end{aligned} \tag{42}$$

Based on the flowchart shown in Fig. 7, six processes are defined as shown in the following.

Process 1: Lasts for $n_1 T_e$ within the PWM period T_s, where n_1 is integer component of $(\mu T_s)/(2T_e)$, defined as $k_1 = n_1$. Execute Case 1 to calculate the next moment state variable according to (39) within each discrete step T_e.

Process 2: Lasts for T_e within the PWM period T_s. Based on Fig. 6, the driving signal exists both 1 and 0 during the time step T_e. Thus, the state variable at the next moment of Case 2 is calculated in two steps, the first is an iterative calculation with duration $(\mu T_s/2)$-$k_1 T_e$ according to (39), and the next is an iterative calculation with duration $k_2 T_e$-$(\mu T_s/2)$ according to (41).

Process 3: Lasts for $n_2 T_e$ within the PWM period T_s, where n_2 is integer component of $[(1\text{-}(\mu/2))T_s\text{-}(k_2 T_e)]/T_e$, defined as $k_3 = k_2 + n_2$. Execute Case 3 to calculate the next moment state variable according to (41) within each discrete step T_e.

Process 4: Similarly with Process 2. Thus, the state variable at the next moment of Case 4 is calculated in two steps, the first is an iterative calculation with duration $(1\text{-}(\mu/2))T_s$-$k_3 T_e$ according to (41), and the next is an iterative calculation with duration $k_4 T_e$-$(1\text{-}(\mu/2))T_s$ according to (39).

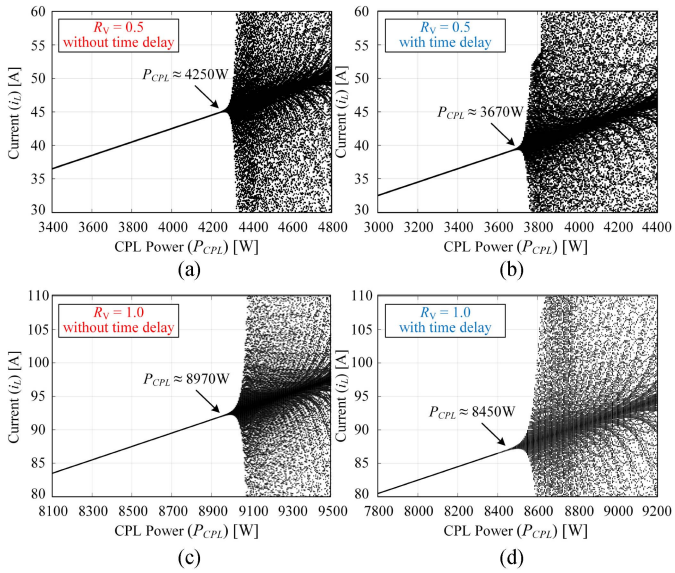

Fig. 8. Bifurcation diagram of inductor current i_L with CPL variation. (a) $R_V = 0.5$ without time delay. (b) $R_V = 0.5$ with time delay. (c) $R_V = 1.0$ without time delay. (d) $R_V = 1.0$ with time delay.

Process 5: Lasts for $n_3 T_e$ within the PWM period T_s, where n_3 is integer component of $(\mu T_s)/(2T_e)$. Execute Case 1 to calculate the next moment state variable according to (39) within each discrete step T_e.

Process 6: When the condition $k = N_e = T_s/T_e$ is satisfied, the PWM period corresponding to discrete state variables and the duty cycle signal obtained by the proposed controller from (24) and (30) are updated.

Remark 6: Considering that in real power systems, the measurement signal sensing of power circuits, analog signal conditioning, and controller duty cycle computation take some time, and thus may result in failure to update synchronously with the PWM carrier. In order to explore the effect of the abovementioned conditions on the stability of the system, we modify the model by introducing time delays in the control variables. For example, if the time delay is less than T_s, as shown in Fig. 6(a), the state variable corresponding to $\mu(n)$ is $X(n\text{-}1)$ instead of $X(n)$, remaining the process unchanged.

In order to explore the large-signal stability of the proposed controller and the effectiveness of virtual damping to suppress CPL oscillations, the CPL power that leads to system instability is used as a bifurcation parameter. The initial RL is 160 Ω, and the detailed circuit parameters and controller parameters are shown in Table II. When the CPL power varies, the inductor current bifurcation diagram of the system converter is presented in Fig. 8.

From Fig. 8(a) and (b), when the system is without time delay, the bifurcation points of the virtual damping $R_V = 0.5$ occur at $P_{CPL} \approx 4250$ W. At this point, the inductor current i_L starts to oscillate with the increase of the CPL power, and this bifurcation point indicates the critical power of CPL. When the system exists time delay resulting in the duty cycle signal update hysteresis, the critical power decreases to 3670 W, which indicates that the time delay is detrimental to the stability of the system.

From Fig. 8(c) and (d), when the virtual damping $R_V = 1.0$, the CPL critical power bifurcation point of the system increases to 8970 and 8450 W without time delay and with time delay, respectively, which validates the capability of the proposed controller to effectively suppress CPL oscillations.

Conclusions4: In order to reduce the detrimental effect of the proposed controller under time delay and CPL, the damping gain R_V should be selected with some margin thus ensuring the large signal stability of the system.

C. Controller Parameter Tuning Guidelines

Considering that the proposed control strategy consists of the PTNDO for source-load side information estimation and the passivity model predictive controller for voltage regulation. Hence, small-signal stability analysis (eigenvalue method) and large-signal stability analysis (Lyapunov and bifurcation diagram method) will be synthesized to provide complete design flow for the proposed controller, which maintains system stability under highly permeable CPL and time delay conditions, while achieving optimal transient performance. Notably, compared to the advanced controllers that were tested through numerical simulations with manual empirical and trial-and-error methods, the selection criteria for the parameters of the proposed controllers are all based on theoretical results.

The parameter design guidelines are summarized as follows.

Step1: Choose T_o and ξ are chosen based on the stability analysis of the Lyapunov function for PTNDO and the upper bound on convergence time derived from (46) (see the Appendix).

Step2: To ensure large-signal stability of the controller used for voltage regulation, the virtual damping R_V at the maximum CPL power of system should be solved according to the bifurcation diagram method based on the discrete-time model of the system in Section IV-B, while keeping some margins for the detrimental effects caused from time delay.

Step3: Based on the stability of step2, to achieve transient performance with minimized overshooting and satisfactory settling time, The R_V should be further determined according to eigenvalue traces based on the Jacobian matrix in Section IV-A.

Remark 7: The stability analysis methods proposed in Section IV-A and IV-B are generalized solution ideas, that can be adapted to existing advanced controllers, thus providing effective assistance in parameter selection.

V. Simulation Results

In this section, the dc microgrid shown in Fig. 1 is built in PLECS and the proposed controller shown in Fig. 3 is simulated and verified. The converter and controller parameters of system are given in Table II. To verify the effectiveness and superiority of the proposed control, not only the verification of convergence characteristics within predefined time, controller parameter sensitivity tests, and large-signal stability are performed, but also adaptive back-stepping control (ABSC) [25], adaptive passivity-based control (APBC) [26], and the proposed APMPC for transient capability comparison. Notably, in order to obtain relatively fair comparisons, we shall use the optimal control parameters of [25] and [26].

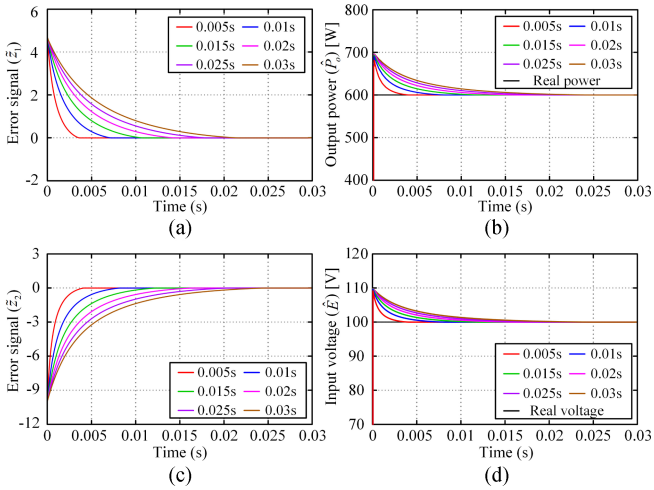

Fig. 9. Performance of the PTNDO when coefficient T_o is assigned different values. (a) Dynamic response of error signal $\tilde{z}_1$. (b) Dynamic response of the estimated output power $\hat{P}_o$. (c) Dynamic response of error signal $\tilde{z}_2$. (d) Dynamic response of the estimated input voltage $\hat{E}$.

A. Case1: Parameter Tuning and Verification of PTNDO

This case mainly studies the convergence performance within predefined time of designing PTNDO based dc microgrid system. The initial startup parameters of the system are input voltage of 100 V and pure CPL 600 W. As can be seen from Fig. 9(a)–(d), the correlation error signals, the output power and the input voltage achieve exact convergence. Meanwhile, the upper bound on the convergence time of PTNDO is always satisfied within different coefficients T_o, which is consistent with the inference of Lemma 1. Although the smaller T_o has a rapid convergence speed, the unavoidable noise and overshooting will cause the system performance to deteriorate. Therefore, a tradeoff between dynamic response and ripple oscillations is necessary. The final coefficients $T_{o1} = 0.01$ and $T_{o2} = 0.02$ are determined, and the simulation results show that the proposed PTNDO is able to achieve accurate estimation of state variables in predefined time.

B. Case2: The Parameter Sensitivity Test for APMPC

In this section, the parameter designs and performance evaluations will be performed by simulation comparison of sensitivity analysis. It is worth noting that the feedback loop of the proposed controller contains only R_V, which greatly reduces the parameter design difficulty. The initial operating conditions of the system are 160 Ω RL and 300 W CPL.

Fig. 10 presents the dynamic response of system for different values of R_V ($R_V = 0.05$, 0.15, 0.5, 1.0, and 1.5) when the CPL is varied from 300 to 600 W. It can be observed that the system oscillates when the APMPC gain R_V is excessively small; with the increase of gain R_V, the system remains stable and the overshoot gradually decreases, but convergence time gradually increases, indicating that the system damping increases, which is consistent with the conclusion of the eigenvalue stability analysis in Section IV-A. However, the measurement noise in real power systems reduces the robustness of the controller, so

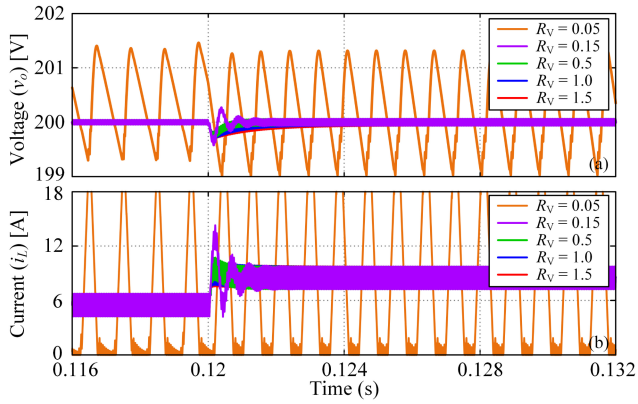

Fig. 10. Dynamic response of system with CPL varying from 300 to 600 W at different value of virtual damping R_V. (a) Output voltage. (b) Inductor current.

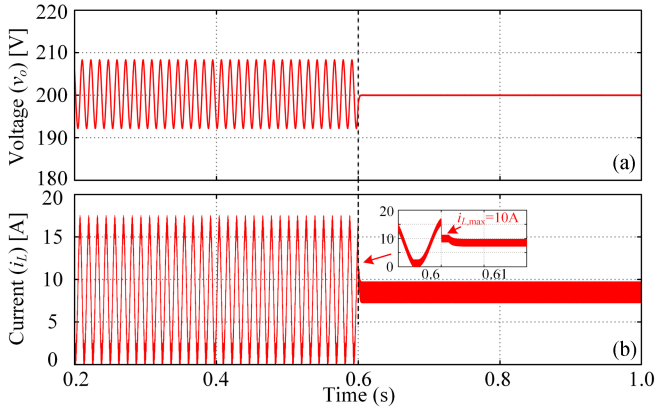

Fig. 11. Dynamic response of switching from open-loop operation to proposed controller. (a) Output voltage. (b) Inductor current.

blindly pursuing fast dynamic response is not desirable. Hence, based on the abovementioned simulation analysis, the trade-off between convergence speed and smoothness of the voltage and inductor current is considered, and the final gain R_V is selected as 1.0.

C. Case3: Large Signal Stability Analysis Verification

This case investigates the capacity of the proposed controller to stabilize the large-signal disturbance limit cycle oscillations induced from the CPL and the maximum CPL power point, respectively, thus validating the results of large-signal stability analysis in Section IV-B.

Fig. 11(a) and (b) present the simulated waveforms of the system switching from open-loop startup to proposed controller at 600 W CPL. We can observe that the system under limit cycle oscillation when operating in open loop with fixed control signal $\mu = 0.5$. At $t = 0.6$ s switching to the proposed controller, the injected virtual damping ensures the energy dissipation, the limit cycle oscillations are restrained, and the inductor current and output voltage are regulated to the equilibrium point within 5 ms. It is worth noting that if the current limiting link is set to 10 A, the inductor current is limited to 10 A at the switching

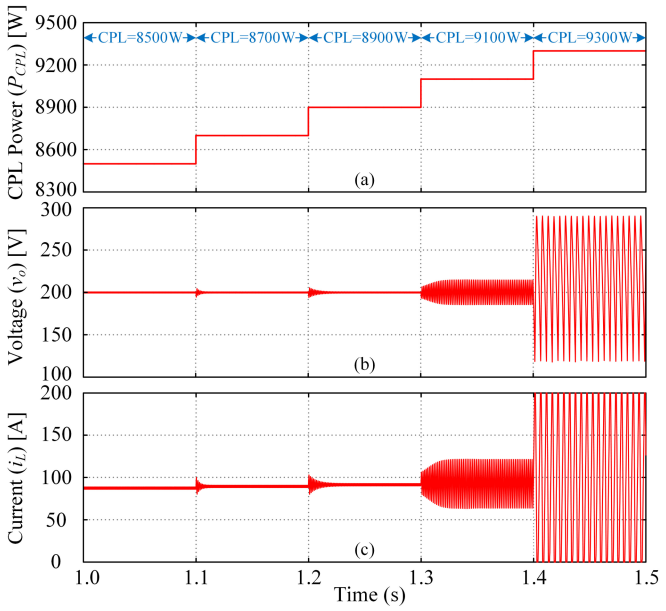

Fig. 12. Dynamic response of the system when P_{CPL} is varied from 8500 to 9300 W with step 200 W. (a) CPL power. (b) Output voltage. (c) Inductor current.

moment until the system is stabilized. The results show that the proposed controller has the ability to stabilize CPL large-signal disturbances and inductor current overshoot limitation.

Fig. 12(b) and (c) present the simulated waveforms of system with CPL power varying from 8500 to 9300 W in 200 W increments. When P_{CPL} varies from 8500 to 8900 W, the output voltage and inductor current of the system are stable. When P_{CPL} varies from 9100 to 9300 W, the output voltage and inductor current both oscillate and gradually increase with the increase of P_{CPL}, which is consistent with the conclusion of large-signal stability analysis in Section IV-B.

D. Case4: Source-Load Side Step Disturbance Test

This case investigates the robustness of different controllers when facing step disturbances on source-load side to verify the superiority of the proposed controller. The simulation process is divided into seven stages.

Stage 1: The initial operating conditions of the system are 100 V input voltage and 300 W pure CPL.

Stage 2: Extra 160 Ω RL access to system at 0.04 s.

Stage 3: Extra 160 Ω RL is removed at 0.08 s.

Stage 4: The CPL power rises from 300 to 800 W at 0.12 s.

Stage 5: The CPL power drops from 800 to 300 W at 0.16 s.

Stage 6: The input voltage drops from 100 to 125 V at 0.20 s.

Stage 7: The input voltage rises from 125 to 75 V at 0.24 s.

From (a) and (b) of Fig. 13, it can be observed that under source-load side step disturbance, the maximum overshoot and the recovery time of the proposed controller are 0.4 V and 2.5 ms, respectively; the maximum overshoot and the recovery time of the APBC proposed in [26] are 3.6 V and 32 ms, respectively; and the maximum overshoot and the recovery time of the ABSC proposed in [25] are 4.6 V and 30 ms, respectively. From

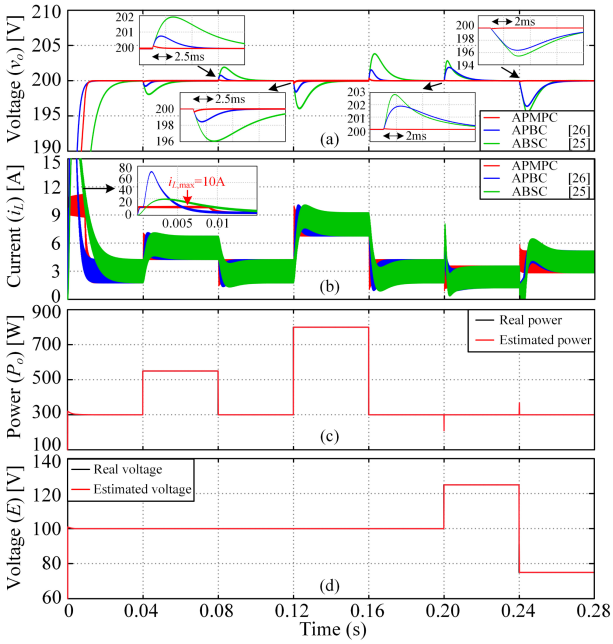

Fig. 13. Dynamic response of the system during step disturbance of source-load side. (a) Output voltage. (b) Inductor current. (c) Estimated output power. (d) Estimated input voltage. For all, APMPC (red line), APBC (blue line), and ABSC (green line).

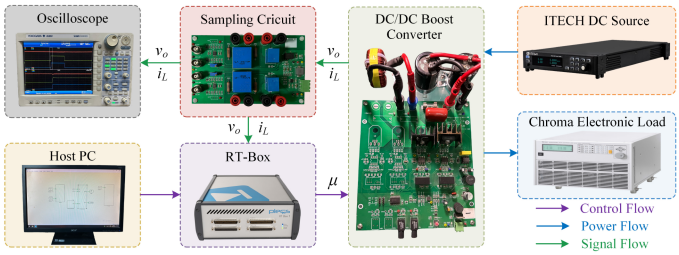

Fig. 14. Experimental platform.

Fig. 13(c) and (d), the designed PTNDO can accurately estimate time-varying input voltage and load power. The simulation results show that all three controllers can stabilize the CPL and achieve accurate regulation, but the transient response of the proposed controller possesses significant advantages, including a smaller overshoot and faster recovery time. Moreover, the inductive current limitation of 10 A during startup significantly reduces the current stress of the device.

VI. Experimental Results

In this section, an experimental prototype as shown in Fig. 14 is constructed in the laboratory to evaluate the effectiveness and superiority of the proposed control algorithm. The device is composed of dc power supply (ITECH IT-M3433 150 V/12 A), an ac/dc electronic load (Chroma 63804 350 V/45 A/4500 W), an oscilloscope (YOKOGAWA DL850), a sampling circuit, a dc/dc boost converter, and an RT-Box. The Chroma electronic loads can be set up as resistive mode or CPL mode for different types of loads. The circuit signals are measured with the LEM's

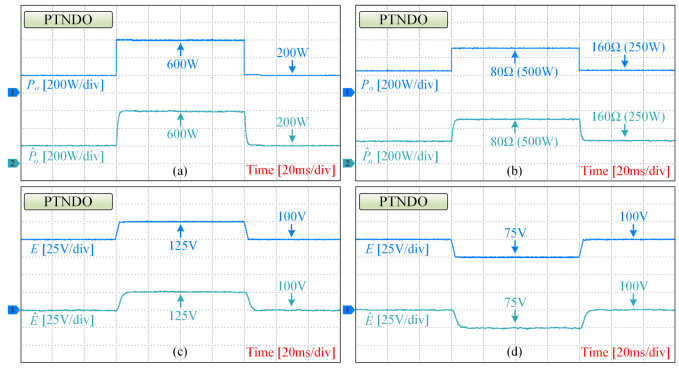

Fig. 15. Experimental results of dynamic response for the proposed PTNDO. (a) CPL step variation (200 W→600 W→200 W). (b) RL step variation (160 Ω→80 Ω→160 Ω). (c) Input voltage step variation (100 V→125 V→100 V). (d) Input voltage step variation (100 V→75 V→100 V).

voltage transducer (LV 25-P) and the LEM's current transducer (HXN 10-P), respectively. The proposed control algorithm is constructed in the PLECS of the host computer and generates the RCP code of RT-BOX, which measures the voltage/current signals through the analog-to-digital converter (ADC) of the RT-BOX and executes the control algorithm to provide 20 kHz PWM signals to dc/dc boost converter. The variation of the source-load side operating conditions is achieved by a programmable dc power supply and an electronic load. In addition, in order to reflect the actual control effect, the system parameters in the experimental platform and the simulation research are kept consistent.

In order to further present the superiority of the controller, we increased the PI controller based on feedback signals in experimental tests. To ensure fairness, the dual-loop parameters were tuned according to design guidelines provided in [39], and eventually selected as $(k_{pv}, k_{iv}, k_{pc}, k_{ic}) = (0.375, 32.5, 0.05, 27.5)$.

A. Experimental Test of the Proposed PTNDO

In this section, the comparison study between the actual and estimated values under the disturbance of source-load side information is performed to assess the validity and accuracy of the proposed PTNDO.

As can be seen from Fig. 15(a) and (b), when the load-side disturbance occurs, whether the load type is CPL or RL, the proposed PTNDO can quickly track this variation by output power, and the observed value of the output power is consistent with the actual value. As can be seen from Fig. 15(c) and (d), when the source-side disturbance occurs, the proposed PTNDO can quickly track this variation, and the observed value of the input voltage agrees with the actual value. The experimental results show that the proposed PTNDO can effectively online observe the source-load side information.

B. Experimental Test of Load (RL and CPL) Changes

In this section, the comparative study is performed in order to assess the robustness and stability of the proposed controllers under multiple types of load disturbances.

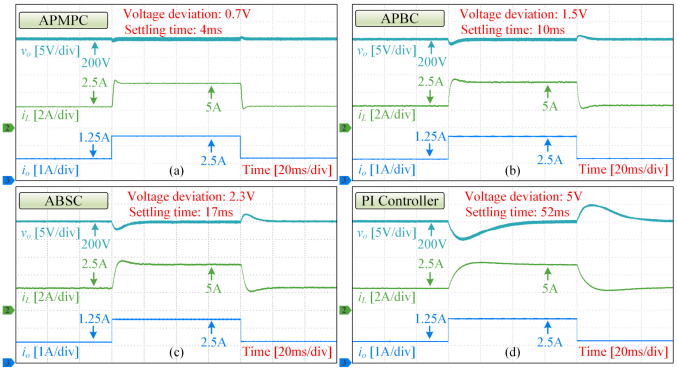

Fig. 16. Experimental comparison results of dynamic response under RL step variation (160 Ω→80 Ω→160 Ω). (a) Proposed APMPC. (b) APBC of [26]. (c) ABSC of [25]. (d) PI controller.

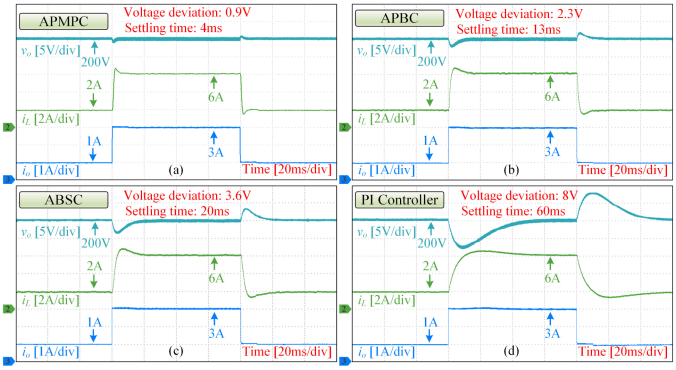

Fig. 17. Experimental comparison results of dynamic response under CPL step variation (200 W→600 W→200 W). (a) Proposed APMPC. (b) APBC of [26]. (c) ABSC of [25]. (d) PI controller.

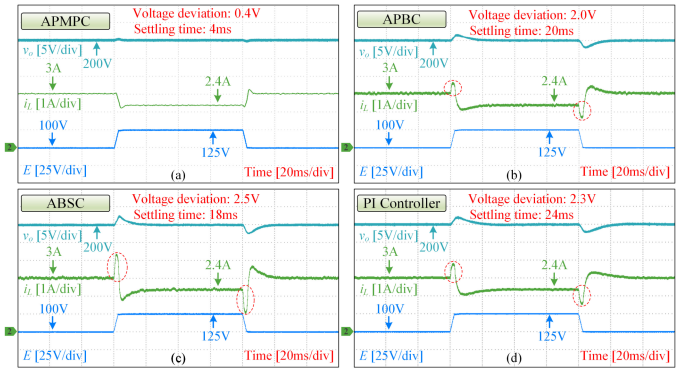

Fig. 18. Experimental comparison results of dynamic response under input voltage step variation (100 V→125 V→100 V). (a) Proposed APMPC. (b) APBC of [26]. (c) ABSC of [25]. (d) PI controller.

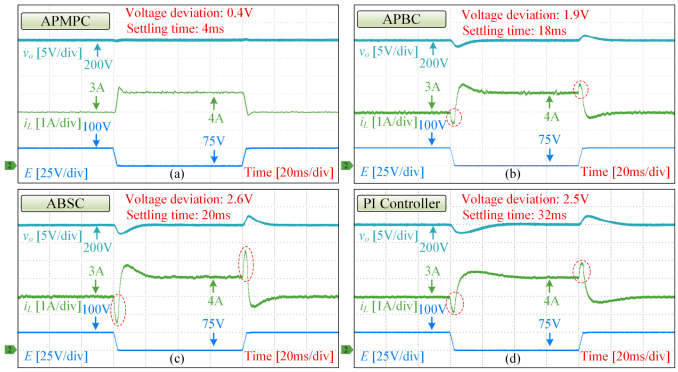

Fig. 19. Experimental comparison results of dynamic response under input voltage step variation (100 V→75 V→100 V). (a) Proposed APMPC. (b) APBC of [26]. (c) ABSC of [25]. (d) PI controller.

In the first case, the RL of the system varies from: 160 Ω→80 Ω→160 Ω. Fig. 16 depicts the comparative experimental waveforms of the RL variation. As can be observed, the proposed method can quickly stabilize the bus voltage with smaller voltage overshoot (0.7 V) and shorter settling time (4 ms). However, by employing APBC in [26], ABSC in [25], and PI control the overshoot and settling time are increased to 1.5, 2.3, 5 V and 10, 17, 52 ms, respectively.

In the latter case, the CPL of the system varies from: 200 W→600 W→200 W. Fig. 17 depicts the comparative experimental waveforms of the CPL variation. As is observed, the proposed method still exhibits desirable control performance while the voltage overshoot is 0.9 V and the settling time is 4 ms. However, the voltage overshoot and the settling time of the other three candidate controllers are increased to 2.3, 3.6, 8 V and 13, 20, 60 ms, respectively. The experimental results show that the proposed controller is robust against load disturbances.

C. Experimental Test of Input Voltage Changes

In this section, the comparative study is performed in order to assess the robustness and stability of the proposed controllers under input voltage disturbances.

In the first case, the input voltage of the system varies from: 100 V→125 V→100 V. Fig. 18 depicts the comparative experimental waveforms of the input voltage variation. As can be observed, the proposed method can quickly stabilize the bus voltage with smaller voltage overshoot (0.4 V) and shorter settling time (4 ms). However, by employing APBC in [26], ABSC in [25], and conventional PI control, the voltage overshoot and settling time are increased to 2.0, 2.5, 2.3 V and 20, 18, 24 ms, respectively.

In the latter case, the input voltage of the system varies from: 100 V→75 V→100 V. Fig. 19 depicts the comparative experimental waveforms of the input voltage variation. As is observed, the proposed method still exhibits desirable control performance while the voltage overshoot is 0.4 V and the settling time is 4 ms. However, the voltage overshoot and the settling time of the other three candidate controllers are increased to 1.9, 2.6, 2.5 V and 18, 20, 32 ms, respectively. It is worth noting that the three candidate controllers produce reverse overshoot of inductor currents at the moment of disturbance, while the inductor currents of the proposed controllers stabilize with a relatively smooth state, which indicates that the proposed PTNDO can effectively estimate and compensate the input voltage online in

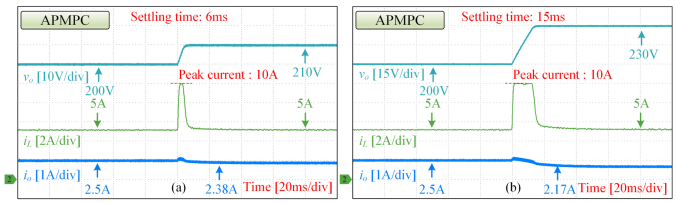

Fig. 20. Experimental results of dynamic response under output voltage reference variation. (a) v_{ref} from 200 to 210 V. (b) v_{ref} from 200 to 230 V.

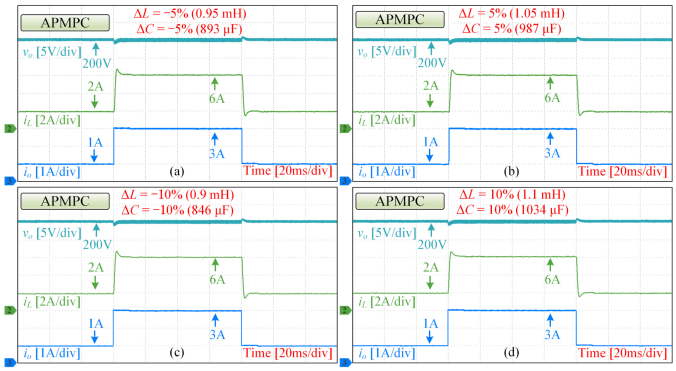

Fig. 21. Experimental results of dynamic response with uncertain inductance and capacitance values. (a) $\Delta L = -5\%$ and $\Delta C = -5\%$. (b) $\Delta L = 5\%$ and $\Delta C = 5\%$. (c) $\Delta L = -10\%$ and $\Delta C = -10\%$. (d) $\Delta L = 10\%$ and $\Delta C = 10\%$.

time. The experimental results show that the proposed controller has excellent robustness against the input voltage disturbances.

D. Experimental Test of Output Voltage Reference Changes

In the experiment, the converter output voltage reference is step changed from 200 to 210 V and 230 V, respectively. The initial CPL power is fixed at 500 W. As can be seen from Fig. 20(a) and (b), the output voltage of converter quickly tracks the new reference value within 6 and 10 ms, respectively, without any voltage overshoot. Moreover, the proposed controller can limit the peak inductor current to the preset $i_{L,\max} = 10$ A. Since the load side is the pure CPL, the steady-state inductor current is unchanged while the output current is reduced correspondingly. The experimental results show that the proposed controller has good voltage regulation capability.

E. Experimental Test of Robustness to Parameter Uncertainty

Considering the practical application of power systems, the quality of components varies and can cause parameter drift with increasing operating time. Thus, to ensure the stable operation of the system over wide operating conditions, the robustness of the proposed controller to parameter uncertainty is investigated in this section. First, the controller inductance and capacitance values are set with deviations in RT-Box. Then, the robustness of the proposed controller is verified under load disturbance.

From the experimental results in Fig. 21, under all parameter drifts, the output voltage and inductor current of the system exhibit the fast dynamic response and small overshoot with the disturbance variations of the CPL. Therefore, under the proposed controller, the uncertainties of inductance and capacitance hardly affect system performance and show good robustness.

TABLE III
EXPERIMENTAL PERFORMANCE METRICS COMPARISON RESULTS

Controller	Test type	Maximum deviation	Settling time
APMPC	Case B load-side disturbance	0.7 V, 0.9 V	4 ms, 4 ms
APBC		1.5 V, 2.3 V	10 ms, 13 ms
ABSC		2.3 V, 3.6 V	17 ms, 20 ms
PI		5.0 V, 8.0 V	52 ms, 60 ms
APMPC	Case C source-side disturbance	0.4 V, 0.4 V	4 ms, 4 ms
APBC		2.0 V, 1.9 V	20 ms, 18 ms
ABSC		2.5 V, 2.6 V	18 ms, 20 ms
PI		2.3 V, 2.5 V	24 ms, 32 ms

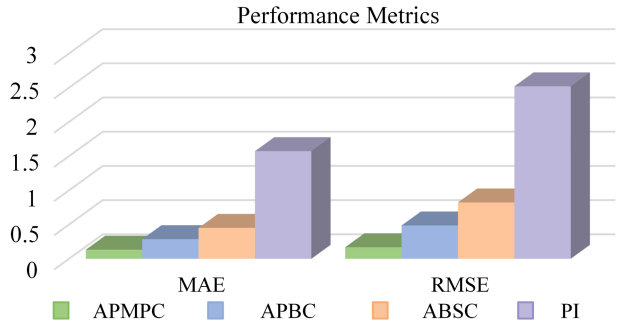

Fig. 22. Quantitative comparative analysis of controllers.

F. Experimental Performance Metrics Analysis

To evaluate the capability of the proposed controllers, an analysis of the performance metrics is conducted. For fairer comparisons, the parameters of the candidate controllers are consistent with the comparison articles [25] and [26]. First, the dynamic performance metrics (maximum overshoot and settling time) of four controllers under different operating conditions were compared, and the results are shown in Table III. In addition, to quantitatively evaluate the performance metrics of the controllers, the mean absolute error (MAE) and root-mean-square-error are comparatively demonstrated through bar charts, and the results are shown in Fig. 22. Combining the abovementioned results, it is clear that the proposed controller offers significant advantages.

VII. CONCLUSION

In this article, an APMPC was proposed to quickly stabilize the dc–dc boost converter for feeding CPLs in dc microgrids. The proposed control strategy mainly combines PBC, MPC, and observer techniques. A PTNDO was first designed to provide accurate estimation of time-varying and unknown load power and input voltage within predefined time. Next, based on the estimated state variables, an adaptive controller that combines two control strategies adopts the advantages of both, and compensates for the weaknesses of each is proposed to significantly improve the robustness and stability of the system.

Then, the system stability is comprehensively analyzed through small-signal and large-signal methods, and the parameter design guidelines of the controller and the CPL critical point under time delay are explored. Moreover, the proposed composite control loop avoids the need for nominal parameters to be acquired and the multiple degrees-of-freedom parameter tuning complexity, and thus has a relatively simple and practical control structure. To further assess the superiority of the proposed control over other prevalent methods, the comparative of simulations and experiments was performed.

APPENDIX

Lemma 1: Consider an autonomous nonlinear system

$$\dot{x} = f(t,x), x(0) = x_0, f(0) = 0, x \in \mathbb{R}^n. \tag{43}$$

Construct positive definite Lyapunov function $V(x)$ satisfies

$$\dot{V}(x) \leq -2\left(2\alpha' V(x) + \alpha_1 V^{1-\frac{\xi}{2}}(x) + \alpha_2 V^{1+\frac{\xi}{2}}(x)\right) \Big/ \xi T_o \alpha' \tag{44}$$

where $0 < \xi < 1, T_o > 0, \alpha_1 > 0, \alpha_2 > 0$ and $\alpha' = \sqrt{\alpha_1 \alpha_2} > 0$. Integrating the both sides of (44) yields

$$\int_0^{T(x_0)} dt \leq \int_{V(x_0)}^{0} -\frac{\xi T_o \alpha'}{2\left(2\alpha' V(x) + \alpha_1 V^{1-\frac{\xi}{2}}(x) + \alpha_2 V^{1+\frac{\xi}{2}}(x)\right)} dV. \tag{45}$$

Then the equilibrium of the system (43) is stable within predefined time, and the bounded settling time satisfies

$$T(x_o) \leq T_o \cdot \left(1 - \left(1 \Big/ \left(1 + \sqrt{\tfrac{\alpha_2}{\alpha_1}} V^{\frac{\xi}{2}}(x_o)\right)\right)\right), \forall x_o \in \mathbb{R}^n. \tag{46}$$

REFERENCES

[1] T. Dragičević, X. Lu, J. C. Vasquez, and J. M. Guerrero, "DC microgrids—Part I: A review of control strategies and stabilization techniques," *IEEE Trans. Power Electron.*, vol. 31, no. 7, pp. 4876–4891, Jul. 2016.

[2] I. Santana and I. G. Zurbriggen, "Dual-loop estimation based adaptive controller for microgrid connected boost converters," *IEEE Trans. Power Electron.*, vol. 40, no. 1, pp. 551–562, Jan. 2025.

[3] X. Wang, J. Huang, Z. Xu, C. Zhang, and X. Guan, "Real-world scale deployment of hydrogen-integrated microgrid: Design and control," *IEEE Trans. Sustain. Energy*, vol. 15, no. 4, pp. 2380–2392, Oct. 2024.

[4] L. Xu et al., "A review of DC shipboard microgrids—Part I: Power architectures, energy storage, and power converters," *IEEE Trans. Power Electron.*, vol. 37, no. 5, pp. 5155–5172, May 2022.

[5] A. Kwasinski and C. N. Onwuchekwa, "Dynamic behavior and stabilization of DC microgrids with instantaneous constant-power loads," *IEEE Trans. Power Electron.*, vol. 26, no. 3, pp. 822–834, Mar. 2011.

[6] A. Emadi, A. Khaligh, C. H. Rivetta, and G. A. Williamson, "Constant power loads and negative impedance instability in automotive systems: Definition, modeling, stability, and control of power electronic converters and motor drives," *IEEE Trans. Veh. Technol.*, vol. 55, no. 4, pp. 1112–1125, Jul. 2006.

[7] P. Lin, C. Zhang, P. Wang, and J. Xiao, "A decentralized composite controller for unified voltage control with global system large-signal stability in DC microgrids," *IEEE Trans. Smart Grid.*, vol. 10, no. 5, pp. 5075–5091, Sep. 2019.

[8] M. Cespedes, L. Xing, and J. Sun, "Constant-power load system stabilization by passive damping," *IEEE Trans. Power Electron.*, vol. 26, no. 7, pp. 1832–1836, Jul. 2011.

[9] A. Hosseinipour and H. Hojabri, "Small-signal stability analysis and active damping control of DC microgrids integrated with distributed electric springs," *IEEE Trans. Smart Grid*, vol. 11, no. 5, pp. 3737–3747, Sep. 2020.

[10] J. Sun, J. Xia, S. Ding, and X. Yu, "Exact-feedback-linearization-based adaptive second-order sliding mode control design for DC–DC boost converters," *IEEE Trans. Ind. Electron.*, to be published, doi: 10.1109/TIE.2024.3476994.

[11] W. He and R. Ortega, "Design and implementation of adaptive energy shaping control for DC–DC converters with constant power loads," *IEEE Trans. Ind. Inform.*, vol. 16, no. 8, pp. 5053–5064, Aug. 2020.

[12] A. Viswambharan, R. Errouissi, M. Debouza, and H. Shareef, "Experimental verification of disturbance observer-based backstepping control for DC–DC boost converter," *IEEE Trans. Circuits Syst. I: Reg. Papers*, vol. 70, no. 12, pp. 5520–5533, Dec. 2023.

[13] H. Lin, H. S.-H. Chung, R. Shen, and Y. Xiang, "Enhancing stability of DC cascaded systems with CPLs using MPC combined with NI and accounting for parameter uncertainties," *IEEE Trans. Power Electron.*, vol. 39, no. 5, pp. 5225–5238, May 2024.

[14] Y. Li, S. Sahoo, T. Dragičević, Y. Zhang, and F. Blaabjerg, "Stability-oriented design of model predictive control for DC/DC boost converter," *IEEE Trans. Ind. Electron.*, vol. 71, no. 1, pp. 922–932, Jan. 2024.

[15] B. A. Martinez-Treviño, A. El Aroudi, A. Cid-Pastor, and L. MartinezSalamero, "Nonlinear control for output voltage regulation of a boost converter with a constant power load," *IEEE Trans. Power Electron.*, vol. 34, no. 11, pp. 10381–10385, Nov. 2019.

[16] C. Cui, N. Yan, B. Huangfu, T. Yang, and C. Zhang, "Voltage regulation of DC–DC buck converters feeding CPLs via deep reinforcement learning," *IEEE Trans. Circuits Syst. II: Express Briefs.*, vol. 69, no. 3, pp. 1777–1781, Mar. 2022.

[17] T. Qie, X. Zhang, W. Jiang, J. Ye, H. H. C. Iu, and T. Fernando, "A novel data-driven large signal stabilizer for interleaved DC/DC boost converter with constant power load," *IEEE Trans. Ind. Electron.*, vol. 71, no. 11, pp. 14308–14317, Nov. 2024.

[18] Q. Xu, N. Vafamand, L. Chen, T. Dragičević, L. Xie, and F. Blaabjerg, "Review on advanced control technologies for bidirectional DC/DC converters in DC microgrids," *IEEE J. Emerg. Sel. Topics Power Electron.*, vol. 9, no. 2, pp. 1205–1221, Apr. 2021.

[19] M. A. Hassan et al., "DC shipboard microgrids with constant power loads: A review of advanced nonlinear control strategies and stabilization techniques," *IEEE Trans. Smart Grid.*, vol. 13, no. 5, pp. 3422–3438, Sep. 2022.

[20] O. Andrés-Martínez, A. Flores-Tlacuahuac, O. F. Ruiz-Martinez, and J. C. Mayo-Maldonado, "Nonlinear model predictive stabilization of DC–DC boost converters with constant power loads," *IEEE J. Emerg. Sel. Topics Power Electron.*, vol. 9, no. 1, pp. 822–830, Feb. 2021.

[21] H. G. Narm, S. Eren, and M. Karimi-Ghartemani, "A robust controller with integrated plant dynamics for constant power loads in DC MicroGrid," *IEEE Trans. Power Electron.*, vol. 38, no. 4, pp. 4419–4429, Apr. 2023.

[22] Q. Guo, M. J. Carrizosa, A. Iovine, and A. Arzandé, "Dynamic feedback linearization and singular perturbation for a stabilizing controller for DC/DC boost converters: Theory and experimental validation," *IEEE Trans. Ind. Electron.*, vol. 71, no. 8, pp. 9559–9568, Aug. 2024.

[23] J. Zeng, Z. Zhang, and W. Qiao, "An interconnection and damping assignment passivity-based controller for a DC–DC boost converter with a constant power load," *IEEE Trans. Ind. Appl.*, vol. 50, no. 4, pp. 2314–2322, Jul./Aug. 2014.

[24] M. Abdolahi, J. Adabi, and S. Y. M. Mousavi, "An adaptive extended Kalman filter with passivity-based control for DC–DC converter in DC microgrids supplying constant power loads," *IEEE Trans. Ind. Electron.*, vol. 71, no. 5, pp. 4873–4882, May 2024.

[25] Q. Xu, C. Zhang, C. Wen, and P. Wang, "A novel composite nonlinear controller for stabilization of constant power load in DC microgrid," *IEEE Trans. Smart Grid.*, vol. 10, no. 1, pp. 752–761, Jan. 2019.

[26] M. A. Hassan, C.-L. Su, F.-Z. Chen, and K.-Y. Lo, "Adaptive passivity-based control of a DC–DC boost power converter supplying constant power and constant voltage loads," *IEEE Trans. Ind. Electron.*, vol. 69, no. 6, pp. 6204–6214, Jun. 2022.

[27] C. Zhang, M. Li, L. Zhou, C. Cui, and L. Xu, "A variable self-tuning horizon mechanism for generalized dynamic predictive control on DC/DC boost converters feeding CPLs," *IEEE J. Emerg. Sel. Topics Power Electron.*, vol. 11, no. 2, pp. 1650–1660, Apr. 2023.
[28] M. Alipour, J. Zarei, R. Razavi-Far, M. Saif, N. Mijatovic, and T. Dragičević, "Observer-based backstepping sliding mode control design for microgrids feeding a constant power load," *IEEE Trans. Ind. Electron.*, vol. 70, no. 1, pp. 465–473, Jan. 2023.
[29] Q. Xu, Y. Yan, C. Zhang, T. Dragicevic, and F. Blaabjerg, "An offset-free composite model predictive control strategy for DC/DC buck converter feeding constant power loads," *IEEE Trans. Power Electron.*, vol. 35, no. 5, pp. 5331–5342, May 2020.
[30] C. Zheng, T. Dragičević, J. Zhang, R. Chen, and F. Blaabjerg, "Composite robust quasi-sliding mode control of DC–DC buck converter with constant power loads," *IEEE J. Emerg. Sel. Topics Power Electron.*, vol. 9, no. 2, pp. 1455–1464, Apr. 2021.
[31] B. Huangfu, C. Cui, C. Zhang, and L. Xu, "Learning-based optimal large-signal stabilization for DC/DC boost converters feeding CPLs via deep reinforcement learning," *IEEE J. Emerg. Sel. Topics Power Electron.*, vol. 11, no. 6, pp. 5592–5601, Dec. 2023.
[32] X. Wang et al., "Toward balancing dynamic performance and system stability for DC microgrids: A new decentralized adaptive control strategy," *IEEE Trans. Smart Grid*, vol. 13, no. 5, pp. 3439–3451, Sep. 2022.
[33] N. Sarrafan et al., "A novel fast fixed-time backstepping control of DC microgrids feeding constant power loads," *IEEE Trans. Ind. Electron.*, vol. 70, no. 6, pp. 5917–5926, Jun. 2023.
[34] Y. Song, H. Ye, and F. L. Lewis, "Prescribed-time control and its latest developments," *IEEE Trans. Syst., Man, Cybern., Syst.*, vol. 53, no. 7, pp. 4102–4116, Jul. 2023.
[35] X. Wang et al., "Adaptive voltage-guaranteed control of DC/DC-buck-converter-interfaced DC microgrids with constant power loads," *IEEE Trans. Ind. Electron.*, vol. 71, no. 11, pp. 14926–14936, Nov. 2024.
[36] L. Ding and C. K. Tse, "Large-signal stability analysis of DC distribution systems with cascading converter structure," *IEEE Trans. Ind. Electron.*, vol. 70, no. 9, pp. 9103–9111, Sep. 2023.
[37] X. Geng, B. Zhang, D. Qiu, Y. Chen, W. Xiao, and F. Xie, "Modeling and nonlinear dynamic analysis of a photovoltaic system with multiple parallel branches based on simplified discrete time model," *IEEE Trans. Power Electron.*, vol. 39, no. 8, pp. 10226–10238, Aug. 2024.
[38] L. Saublet, R. Gavagsaz-Ghoachani, J. Martin, B. Nahid-Mobarakeh, and S. Pierfederici, "Bifurcation analysis and stabilization of DC power systems for electrified transportation systems," *IEEE Trans. Transp. Electrific.*, vol. 2, no. 1, pp. 86–95, Mar. 2016.
[39] P. Lin, P. Wang, J. Xiao, J. Wang, C. Jin, and Y. Tang, "An integral droop for transient power allocation and output impedance shaping of hybrid energy storage system in DC microgrid," *IEEE Trans. Power Electron.*, vol. 33, no. 7, pp. 6262–6277, Jul. 2018.

Zehua Zhang (Student Member, IEEE) received the M.S. degree in electrical engineering from the Hebei University of Technology, Tianjin, China, in 2023. He is currently working toward the Ph.D. degree in electrical engineering with the Harbin Institute of Technology, Harbin, China.

His current research interests include DC microgrids, advanced control, and power electronics.

Panbao Wang (Senior Member, IEEE) received the M.S. and Ph.D. degrees in electrical engineering from the Harbin Institute of Technology (HIT), Harbin, China, in 2011 and 2016, respectively.

In 2017, he joined the Department of Electrical Engineering, HIT, as an Assistant Professor. Since 2020, he has been an Associate Professor with the Department of Electrical Engineering, HIT. His research interests include distributed control and optimal operation of microgrids, highly integrated power electronics converters, etc.

Jiyao Zhou was born in Xuchang, China. He received the M.S. degree in biomedical engineering and the Ph.D. degree in electric engineering from the Hebei University of Technology, Tianjin, China, in 2016 and 2022, respectively.

He is currently working with the State Grid International Development Company, Ltd., Beijing, China. His research interests include the power market, secondary advanced control of the dc microgrid system, nonlinear control of microgrid, etc.

Wei Wang (Member, IEEE) received the B.S. degree in automatic test and control, the M.S. degree in electrical engineering, and the Ph.D. degree in mechanical electronic engineering from the Harbin Institute of Technology (HIT), Harbin, China, in 1984, 1990, and 2002, respectively.

Since 2003, she has been a Professor with the Department of Electrical Engineering, HIT. Her research interests include soft-switching converters, photovoltaic grid-connected inverters, and ac/dc microgrids.

Dianguo Xu (Fellow, IEEE) received the B.S. degree in control engineering from Harbin Engineering University, Harbin, China, in 1982, and the M.S. and Ph.D. degrees in electrical engineering from the Harbin Institute of Technology (HIT), Harbin, China, in 1984 and 1989, respectively.

In 1984, he joined the Department of Electrical Engineering, HIT, as an Assistant Professor. Since 1994, he has been a Professor with the Department of Electrical Engineering, HIT. From 2000 to 2010, he was the Dean with the School of Electrical Engineering and Automation, HIT. From 2014 to 2020, he was the Vice President of HIT. He has authored or coauthored more than 1000 technical papers. His research interests include renewable energy generation technology, power quality mitigation, sensorless vector-controlled motor drives, and high-performance PMSM servo system.

Dr. Xu is an Associate Editor for IEEE TRANSACTIONS ON POWER ELECTRONICS, IEEE TRANSACTIONS ON INDUSTRIAL ELECTRONICS, and IEEE JOURNAL OF EMERGING AND SELECTED TOPICS IN POWER ELECTRONICS. He serves as the Chairman of the IEEE Harbin Section. He was the recipient of the 2018 IEEE Industry Applications Society Outstanding Achievement Award.